A Discontinuous Enrichment Method for Capturing Evanescent Waves in Multi-scale Fluid and Fluid/Solid Problems

Radek Tezaur, Lin Zhang, Charbel Farhat *

Department of Mechanical Engineering and Institute for Computational and Mathematical Engineering, Stanford University, Mail Code 3035, Stanford, CA 94305, U.S.A.

Abstract

An evanescent wave is produced when a propagating incident wave impinges on an interface between two media or materials at a sub-critical angle. The sub-scale nature of such a wave makes it difficult to be captured computationally. In this paper, the Discontinuous Enrichment Method (DEM) developed in [1–7] is extended to a class of evanescent wave problems. New DEM elements are constructed by enriching polynomial approximations with free-space evanescent solutions in order to achieve high accuracy for problems with fluid/fluid or fluid/solid interfaces on which evanescent waves may occur. The new DEM elements are applied to the solution of various two-dimensional model problems with evanescent waves. Their performance is observed to be better than that of the basic Helmholtz type DEM elements, and superior to that of the classical higher-order polynomial finite element method.

Key words: discontinuous Galerkin, enrichment, evanescent waves, Helmholtz, Lagrange multipliers, medium frequency, multiscale, wave propagation

1. Introduction

Wave propagation phenomena occur in many physical systems of engineering interest. Sound waves, water waves, and seismic waves are studied in acoustics and mechanics. Another

* Corresponding author.
Email address: cfarhat@stanford.edu (Charbel Farhat).

important class of waves arises in electro-magnetics. A vast amount of literature exists on the general topic of wave propagation and its many applications (for example, see [8–15] and the references cited therein). Whichever the underlying physical phenomenon is, some important attributes are shared by most wave propagation problems, one of which is the computational complexity required to solve them. As the frequency of the waves or the size of the computational domain grows, the problem becomes more challenging computationally, eventually becoming intractable using traditional discretization methods.

In this paper, we concentrate on a multiscale aspect of harmonic wave propagation that occurs in layered media. When a propagating wave impinges on an interface between two materials, some part of the energy is reflected back into the first material and another part penetrates into the second material giving rise to a refracted wave. When the angle of incidence of the impinging wave is below a critical value, all of the energy is reflected back: this is called *total internal reflection*. Even though no energy is transmitted through the interface, a disturbance is still produced at the other side of the interface. This disturbance, which can be viewed as a small-scale feature of wave propagation, is called an *evanescent wave*.

The evanescent waves were described by Isaac Newton almost four hundred years ago [16]. Later, they have been studied by many other scientists (for example, see [17, 18]). Typically, they decay exponentially away from an interface. Being a localized phenomenon, they have recently attracted a lot of attention as technology expanded into the nano-world. For example, a wide range of devices have been invented with the application of electromagnetic evanescent waves, including a fingerprint sensor [19] and various chemical and biological sensors [16]. Other applications of evanescent waves can also be found in the development of nanotechnologies [20], acoustic wave devices [21], detection of buried objects [22], etc.

To illustrate the challenge posed by evanescent waves for a numerical solution method, Figure 1 shows an example of an evanescent acoustic wave that occurs at an interface between two fluids Ω_1 and Ω_2 characterized by two different speeds of sound c_1 and $c_2 > c_1$, when an incident wave hits the interface at a sub-critical angle of incidence. For comparison, Figure 2 shows the refracted plane wave that occurs at the same interface but for a super-critical value of the angle of incidence. Compared to the large-scale wave propagating in Ω_1, the evanescent wave is a small-scale feature which rapidly decays in Ω_2 away from the interface. It can be shown that the decay in the direction perpendicular to the interface is exponential and thus can lead to a very high gradient of the evanescent wave solution. In the direction along the interface, the evanescent solution in Ω_2 oscillates with a wavelength that can be as short as that of the fluid with the lower speed of sound (Ω_1). Thus, capturing in a numerical computation the evanescent wave in Ω_2 may require a fine mesh along the interface, even when the wave number in this fluid is so low that, as suggested by Figure 2, a coarse mesh suffices to capture the refracted wave when the angle of incidence is super-critical.

There are two possible approaches for handling the sub-grid characteristics of evanescent waves. One approach is to use graded meshes, which results in a large number of degrees of freedom and possibly incurs prohibitive costs. The other approach is to enrich the approx-

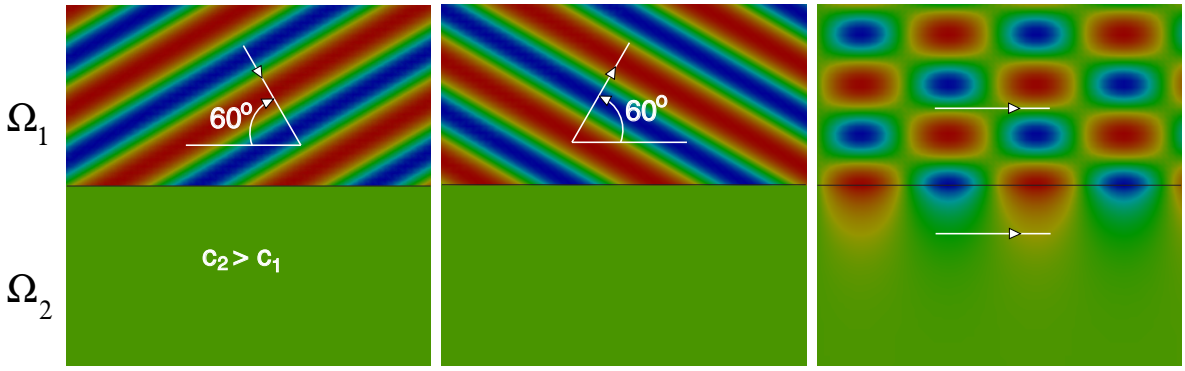

(a) (b) (c)

Fig. 1. Example of an evanescent wave. The upper half domain Ω_1 is air, the lower half Ω_2 is water, and the interface is marked by a black horizontal line. The critical angle is $\theta_{\text{cr}} = 77.16^o$. (a) The incident wave propagating in air at the angle $\theta_{\text{inc}} = 60^o$ toward to the interface, (b) the reflected wave in air, and (c) the superposition of the incident and reflected waves in air and the evanescent wave in water.

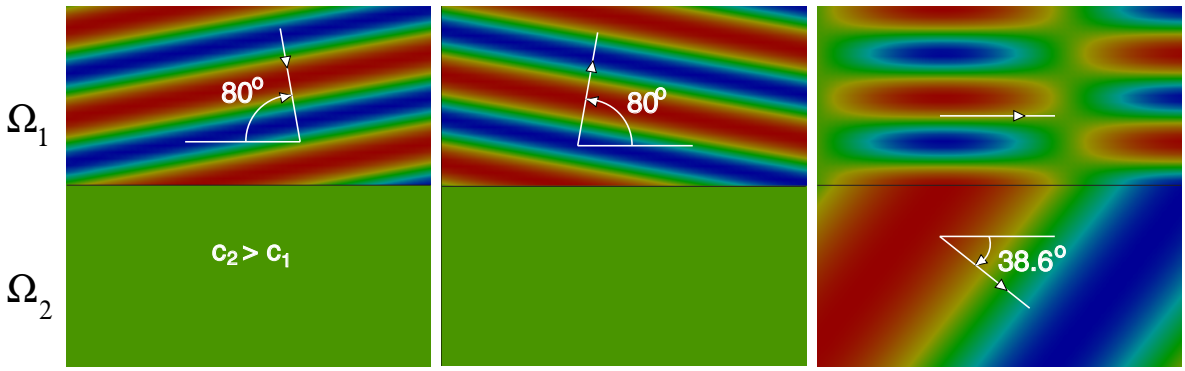

(a) (b) (c)

Fig. 2. Example of a refracted plane wave. The upper half domain Ω_1 is air, the lower half Ω_2 is water, and the interface is marked by a black horizontal line. The critical angle is $\theta_{\text{cr}} = 77.16^o$. (a) The incident wave propagating in air at the angle $\theta_{\text{inc}} = 80^o$ toward to the interface, (b) the reflected wave in air, and (c) the superposition of the incident and reflected waves in air and the refracted plane wave propagating in water at the angle $\theta_t = 38.6^o$.

imation spaces with special functions. This is the idea adopted in this paper for capturing numerically the characteristics of evanescent waves.

The idea of using special, problem dependent approximation functions has been used by a number of finite element techniques, both in the context of wave propagation and other multiscale problems. These include the generalized finite element method (GFEM) [23–26], the extended finite element method (XFEM) [27, 28], the *hp* cloud method [29, 30], the least squares method [31], the weak element method [32], the ultra-weak method [32], the variational theory of complex rays [33], and the discontinuous enrichment method (DEM) [1–7].

The discontinuous enrichment method, which will be used in this paper, differs from the other approaches mentioned above in several ways. It approximates the solution of the prob-

lem by the sum of a continuous polynomial field and an enrichment field that is typically discontinuous at the interfaces between elements. It also enforces a weak continuity between elements through Lagrange multipliers. As such, it is cast in a hybrid variational setting. The enrichment functions are chosen as the free-space solutions of the homogeneous part of the given problem. The Lagrange multiplier field is chosen accordingly. DEM was first proposed in [1] for the solution of problems with sharp gradients and rapid oscillations. In [2], it was developed for the Helmholtz equation. In this case, it was shown that for a large class of Helmholtz problems, the polynomial part of the approximation is not necessary for capturing the solution efficiently. Thus, by dropping the polynomial field from the approximation, DEM was transformed into a non-standard Discontinuous Galerkin Method (DGM) where a weak continuity of the approximation is enforced by Lagrange multipliers. DEM/DGM was further developed in [3–7] where excellent performance has been demonstrated for multiscale problems, elastic wave propagation, and both two-dimensional and three-dimensional acoustic scattering problems. In this paper, DEM is formulated for a computational domain that contains two media or materials whereby the solution may include evanescent waves. Then, *sample* new DEM elements are constructed for capturing the characteristics of these sub-grid scale waves.

The remainder of this paper is organized as follows. Section 2 presents the mathematical formulation of model acoustic problems with a fluid/fluid or fluid/solid planar interface, and a corresponding hybrid variational framework. In Section 3, Snell's law is revisited and evanescent solutions for fluid/fluid and fluid/solid problems are reviewed. Sample new DEM elements for multiscale wave problems are constructed in Section 4 and their performance is assessed in Section 5 in the medium frequency regime. Finally, conclusions are presented in Section 6.

2. Mathematical formulation

Here, two common problems whose solutions can be in the form of evanescent waves are considered. The first problem includes a planar interface between two fluids characterized by two different speeds of sound. The second problem is designed around a fluid/solid planar interface. In each case, the mathematical formulation of the problem is presented and followed by a corresponding hybrid variational formulation.

2.1. Fluid/fluid model wave propagation problem

2.1.1. Boundary value problem

Consider a wave propagation problem defined in a two-dimensional bounded domain Ω filled with two homogeneous ideal fluids in subdomains Ω_1 and Ω_2, respectively, i.e. $\Omega = \Omega_1 \bigcup \Omega_2$. Let $\partial\Omega_m$ denote the boundary of subdomain $\Omega_m, m = 1, 2$, and $\Gamma_0 = \partial\Omega_1 \bigcap \partial\Omega_2$ the planar

interface between the two subdomains. The outer boundaries are denoted by $\Gamma_1 = \partial\Omega_1 \backslash \Gamma_0$ and $\Gamma_2 = \partial\Omega_2 \backslash \Gamma_0$, respectively.

Assuming the waves are time-harmonic with circular frequency ω, the wave propagation in each subdomain is governed by the Helmholtz equation

$$\Delta p_m + k_m^2 p_m = 0, \quad \text{in} \quad \Omega_m, \quad m = 1, 2, \tag{1}$$

where p_m is the pressure, $k_m = \omega / c_m$ is the wave number, and c_m is the speed of sound in Ω_m, $m = 1, 2$. Equilibrium and compatibility at the interface Γ_0 give the following transmission conditions

$$p_1 = p_2, \qquad \text{on} \quad \Gamma_0, \tag{2}$$

$$\frac{1}{\rho_1} \frac{\partial p_1}{\partial \underline{n}} = \frac{1}{\rho_2} \frac{\partial p_2}{\partial \underline{n}}, \quad \text{on} \quad \Gamma_0, \tag{3}$$

where $\rho_m, m = 1, 2$, are the material density, $\underline{n}$ is the normal direction of the interface, and underlining is used here and throughout the remainder of this paper to denote a vector quantity.

Without loss of generality, the Robin boundary condition is considered, i.e.

$$\frac{\partial p_m}{\partial \underline{n}} - i k_m p_m = g_m, \quad \text{on} \quad \Gamma_m, \quad m = 1, 2, \tag{4}$$

where $i = \sqrt{-1}$ is the imaginary unit, and g_m is the excitation at boundary $\Gamma_m, m = 1, 2$.

2.1.2. Hybrid variational formulation and discretization

Let Ω_m be partitioned into $n_m, m = 1, 2$, elements as follows

$$\bar{\Omega}_m = \bigcup_{j=1}^{n_m} \bar{\tau}_j^m, \qquad \tau_j^m \bigcap \tau_l^m = \emptyset \quad \text{if} \quad j \neq l, \quad j, l = 1, 2, ..., n_m, \quad m = 1, 2, \tag{5}$$

and denote by $\Delta_h^m = \{\tau_j^m\}_{j=1}^{n_m}$ the set of all elements in Ω_m, $m = 1, 2$, where the subscript h refers to the element size. Furthermore, let $\mathcal{U}^m$, $m = 1, 2$, and Λ^m, $m = 0, 1, 2$, denote the following spaces

$$\mathcal{U}^m = \prod_{\tau \in \Delta_h^m} H^1(\tau), \quad \Lambda^m = \prod_{\tau_j \in \Delta_h^m} \prod_{\tau_l \in \Delta_h^m, j<l} H^{-1/2}(\partial\tau_j \bigcap \partial\tau_l), \quad m = 1, 2, \tag{6}$$

$$\Lambda^0 = \prod_{\tau_j \in \Delta_h^2} H^{-1/2}(\Gamma_0 \cap \partial\tau_j). \tag{7}$$

Then, introducing the new variables

$$q_m = \frac{p_m}{\rho_m}, \quad m = 1, 2,$$

the hybrid variational form of the boundary value problem (1)-(4) is as follows.

Find $(q_m, \lambda_m, \lambda_0) \in \mathcal{U}^m \times \Lambda^m \times \Lambda^0$, $m = 1, 2$, *such that*

$$a_m(q_m, \psi) + b_m(\lambda_m, \psi) + c(\lambda_0, \psi) = r_m(\psi), \quad \forall \psi \in \mathcal{U}^m, \quad m = 1, 2, \tag{8}$$
$$b_m(\mu, q_m) = 0, \quad \forall \mu \in \Lambda^m, \quad m = 1, 2, \tag{9}$$
$$\rho_1 c(\mu, q_1) - \rho_2 c(\mu, q_2) = 0, \quad \forall \mu \in \Lambda^0, \tag{10}$$

where the bilinear forms $a_m(\cdot, \cdot)$ are defined on $\mathcal{U}^m \times \mathcal{U}^m$, $m = 1, 2$, as

$$a_m(q_m, \psi) = \sum_{\tau \in \Delta_h^m} \int_\tau (\nabla q_m \cdot \nabla \psi - k_m^2 q_m \psi) dx dy - \sum_{\tau \in \Delta_h^m} \int_{\partial\tau \bigcap \Gamma_m} i k_m q_m \psi ds, \qquad m = 1, 2, \tag{11}$$

$b_m(\cdot, \cdot)$ are defined on $\Lambda^m \times \mathcal{U}^m$, $m = 1, 2$, as

$$b_m(\lambda_m, \psi) = \sum_{\tau_j \in \Delta_h^m} \sum_{\substack{\tau_l \in \Delta_h^m \\ j<l}} \int_{\partial\tau_j \cap \partial\tau_l} \lambda_m (\psi|_{\tau_j} - \psi|_{\tau_l}) ds, \qquad m = 1, 2, \tag{12}$$

$c(\cdot, \cdot)$ is defined on $\Lambda^0 \times (\mathcal{U}^1 \bigcup \mathcal{U}^2)$ as

$$c(\lambda_0, \psi) = \sum_{\tau_j \in \Delta_h^2} \int_{\Gamma_0 \cap \tau_j} \lambda_0 \psi ds, \tag{13}$$

and the linear forms $r_m(\cdot)$, $m = 1, 2$, are defined on $\mathcal{U}^m$, respectively, as

$$r_m(\psi) = \int_{\Gamma_m} \frac{1}{\rho_m} g_m \psi ds, \qquad m = 1, 2. \tag{14}$$

Let $\mathcal{U}_h^m$, Λ_h^m, $m = 1, 2$, and Λ_h^0 be finite dimensional spaces satisfying

$$\mathcal{U}_h^m \subset \mathcal{U}^m, \quad \Lambda_h^m \subset \Lambda^m, \quad m = 1, 2, \qquad \Lambda_h^0 \subset \Lambda^0. \tag{15}$$

The discretization of the variational problem (8)-(10) is obtained by substituting the finite dimensional spaces into the hybrid variation form, i.e.
Find $(q_{m,h}, \lambda_{m,h}, \lambda_{0,h}) \in \mathcal{U}_h^m \times \Lambda_h^m \times \Lambda_h^0$, $m = 1, 2$, *such that*

$$a_m(q_{m,h}, \psi) + b_m(\lambda_{m,h}, \psi) + c(\lambda_{0,h}, \psi) = r_m(\psi), \quad \forall \psi \in \mathcal{U}_h^m, \quad m = 1, 2, \tag{16}$$
$$b_m(\mu, q_{m,h}) = 0, \quad \forall \mu \in \Lambda_h^m, \quad m = 1, 2, \tag{17}$$
$$\rho_1 c(\mu, q_{1,h}) - \rho_2 c(\mu, q_{2,h}) = 0, \quad \forall \mu \in \Lambda_h^0, \tag{18}$$

2.2. Fluid/solid model wave propagation problem

2.2.1. Boundary value problem

Next, the wave propagation problem is formulated in a domain $\Omega = \Omega_f \bigcup \Omega_s$, where Ω_f and Ω_s are fluid and solid subdomains, respectively. For simplicity, the solid material is assumed to be isotropic and linearly elastic.

A time-harmonic elastic wave propagation is governed by Navier's equations [11]

$$\mu_L \Delta \underline{u} + (\lambda_L + \mu_L)\nabla(\nabla \cdot \underline{u}) + \rho_s \omega^2 \underline{u} = -\underline{f}(\underline{x}), \qquad \text{in } \Omega_s. \tag{19}$$

Here, ρ_s is the density of the elastic material, λ_L and μ_L are its Lamé constants, $\underline{f}$ is the body force, and $\underline{u} \equiv \underline{u}(\underline{x})$ is the displacement field in Ω_s.

Let

$$M = \begin{bmatrix} \lambda_L + 2\mu_L & \lambda_L & 0 \\ \lambda_L & \lambda_L + 2\mu_L & 0 \\ 0 & 0 & \mu_L \end{bmatrix} \quad \text{and} \quad D = \begin{bmatrix} \dfrac{\partial}{\partial x} & 0 \\ 0 & \dfrac{\partial}{\partial y} \\ \dfrac{\partial}{\partial y} & \dfrac{\partial}{\partial x} \end{bmatrix}. \tag{20}$$

Then, Navier's equations (19) can also be written concisely as

$$D^T M D \underline{u} + \rho_s \omega^2 \underline{u} = -\underline{f}, \qquad \text{in } \Omega_s, \tag{21}$$

where the superscript T designates the transpose operation.

The wave propagation in the fluid subdomain Ω_f is governed by the Helmholtz equation

$$\Delta p + k^2 p = 0, \qquad \text{in } \Omega_f, \tag{22}$$

where $p \equiv p(\underline{x})$ is the pressure field and k is the wave number in the fluid subdomain Ω_f.

Equilibrium and compatibility at the interface Γ_0 yield the following transmission conditions

$$\rho_f \omega^2 \underline{u} \cdot \underline{n} = \frac{\partial p}{\partial \underline{n}}, \qquad \text{on } \Gamma_0, \tag{23}$$

$$\underline{\underline{\sigma}}(\underline{u})\underline{n} \cdot \underline{n} + p = 0, \qquad \text{on } \Gamma_0, \tag{24}$$

where ρ_f is the density of the fluid, $\underline{n}$ is the normal direction on the fluid/solid interface $\Gamma_0 = \partial\Omega_f \bigcap \partial\Omega_s$ and $\underline{\underline{\sigma}}$ is the stress tensor. Without any loss of generality, the following boundary conditions are considered

$$\underline{\underline{\sigma}}(\underline{u})\underline{n} = \underline{g}_s, \qquad \text{on } \Gamma_s, \tag{25}$$

$$\frac{\partial p}{\partial \underline{n}} - ikp = g_f, \qquad \text{on } \Gamma_f, \tag{26}$$

where $\Gamma_f = \partial\Omega_f \backslash \Gamma_0$, $\Gamma_s = \partial\Omega_s \backslash \Gamma_0$, g_f is the excitation on Γ_f, and $\underline{g}_s$ is the specified traction on Γ_s.

2.2.2. Hybrid variational formulation and discretization

Let Ω_f and Ω_s be partitioned into n_f and n_s elements, respectively, i.e.

$$\overline{\Omega}_f = \bigcup_{j=1}^{n_f} \overline{\tau}_j^f, \qquad \tau_j^f \bigcap \tau_l^f = \emptyset \quad \text{if } j \neq l, \quad j,l = 1,2,...,n_f, \tag{27}$$

$$\overline{\Omega}_s = \bigcup_{j=1}^{n_s} \overline{\tau}_j^s, \qquad \tau_j^s \bigcap \tau_l^s = \emptyset \quad \text{if } j \neq l, \quad j,l = 1,2,...,n_s. \tag{28}$$

Let $\Delta_h^f = \{\tau_j^f\}_{j=1}^{n_f}$ and $\Delta_h^s = \{\tau_j^s\}_{j=1}^{n_s}$ be the set of all elements in Ω_f and Ω_s, respectively. Furthermore, let $\mathcal{U}^f$, Λ^f, $\mathcal{U}^s$ and Λ^s denote the following spaces

$$\mathcal{U}^f = \prod_{\tau \in \Delta_h^f} H^1(\tau), \qquad \Lambda^f = \prod_{\tau_j \in \Delta_h^f} \prod_{\tau_l \in \Delta_h^f, j<l} H^{-1/2}(\partial\tau_j \bigcap \partial\tau_l), \tag{29}$$

$$\mathcal{U}^s = \prod_{\tau \in \Delta_h^s} \Big(H^1(\tau)\Big)^2, \tag{30}$$

$$\Lambda^s = \Big\{ \underline{\lambda} \in \prod_{\tau_j \in \Delta_h^s} \prod_{\substack{\tau_l \in \Delta_h^s \\ j<l}} \Big(H^{-1/2}(\partial\tau_j \bigcap \partial\tau_l)\Big)^2 \quad \text{and} \tag{31}$$

$$\forall \underline{\lambda}|_{\partial\tau_j \bigcap \partial\tau_l} \; \exists \underline{\underline{\sigma}} \in H(div;\Omega_s) \;\; s.t. \;\; \underline{\underline{\sigma}} \cdot \underline{n} = \underline{\lambda} \;\; \text{on} \;\; \partial\tau_j \bigcap \partial\tau_l \Big\},$$

where $H^1(\tau)$ and $H^{-1/2}(\partial\tau)$ are the usual Sobolev spaces [34], and

$$H(div;\Omega_s) = \Big\{ \underline{\underline{\sigma}} \in \Big(L_2(\Omega_s)\Big)^{2\times 2} : \sigma_{jl} = \sigma_{lj}, 1 \leq j,l \leq 2, \; div\underline{\underline{\sigma}} = \Big(\sum_{l=1}^{2} \frac{\partial \sigma_{jl}}{\partial x_l} \Big)_{1 \leq j \leq 2} \in \Big(L_2(\Omega_s)\Big)^2 \Big\}. \tag{32}$$

Then, the hybrid weak form of the boundary value problem (21)-(26) can be written as follows

Find $(p, \lambda^f) \in \mathcal{U}^f \times \Lambda^f$ *and* $(\underline{u}, \underline{\lambda}^s) \in \mathcal{U}^s \times \Lambda^s$ *such that*

$$a_f(p,q) + b_f(\lambda^f, q) + \rho_f \omega^2 c(\underline{u}, q) = r_f(q), \quad \forall q \in \mathcal{U}^f, \tag{33}$$

$$a_s(\underline{u}, \underline{v}) + b_s(\underline{\lambda}^s, \underline{v}) + c(\underline{v}, p) = r_s(\underline{v}), \quad \forall \underline{v} \in \mathcal{U}^s, \tag{34}$$

$$b_f(\mu^f, p) = 0, \qquad \forall \mu^f \in \Lambda^f, \tag{35}$$

$$b_s(\underline{\mu}^s, \underline{u}) = 0, \qquad \forall \underline{\mu}^s \in \Lambda^s, \tag{36}$$

where $a_f(\cdot,\cdot)$ is the bilinear form defined on $\mathcal{U}^f \times \mathcal{U}^f$ as

$$a_f(p,q) = \sum_{\tau\in\Delta_h^f} \int_\tau (\nabla p \cdot \nabla q - k^2 pq) dxdy - \int_{\Gamma_f} ikpqds, \tag{37}$$

$b_f(\cdot,\cdot)$ is defined on $\Lambda^f \times \mathcal{U}^f$ as

$$b_f(\lambda^f, p) = \sum_{\tau_j\in\Delta_h^f} \sum_{\substack{\tau_l\in\Delta_h^f \\ j<l}} \int_{\partial\tau_j\cap\partial\tau_l} \lambda^f (p|_{\tau_j} - p|_{\tau_l}) ds, \qquad m = 1,2, \tag{38}$$

$a_s(\cdot,\cdot)$ and $b_s(\cdot,\cdot)$ are defined on $\mathcal{U}^s \times \mathcal{U}^s$ and $\Lambda^s \times \mathcal{U}^s$, respectively, as

$$a_s(\underline{u},\underline{v}) = \sum_{\tau\in\Delta_h^s} \int_\tau \Big(D\underline{v}\Big)^T M\Big(D\underline{u}\Big)\, dxdy - \rho_s\omega^2 \sum_{\tau\in\Delta_h^s} \int_\tau \underline{u}\cdot\underline{v}\, dxdy, \tag{39}$$

$$b_s(\underline{\lambda},\underline{v}) = \sum_{\tau_j\in\Delta_h^s} \sum_{\substack{\tau_l\in\Delta_h^s \\ j<l}} \int_{\partial\tau_j\cap\partial\tau_l} \underline{\lambda}\cdot(\underline{v}|_{\tau_j} - \underline{v}|_{\tau_l})\, ds, \tag{40}$$

$c(\cdot,\cdot)$ is the coupling term defined on $\mathcal{U}^s \times \mathcal{U}^f$ as

$$c(\underline{u},p) = \int_{\Gamma_0} p(\underline{u}\cdot\underline{n}) ds, \tag{41}$$

and the linear forms $r_f(\cdot)$ and $r_s(\cdot)$ are defined on $\mathcal{U}^f$ and $\mathcal{U}^s$, respectively, as

$$r_f(q) = \int_{\Gamma_f} g_f q ds, \tag{42}$$

$$r_s(\underline{v}) = \int_{\Omega_s} \underline{f}\cdot\underline{v}\, dxdy + \int_{\Gamma_N} \underline{g}_s\cdot\underline{v}\, ds. \tag{43}$$

Let $\mathcal{U}_h^f$, Λ_h^f, $\mathcal{U}_h^s$ and Λ_h^s be finite dimensional spaces satisfying

$$\mathcal{U}_h^f \subset \mathcal{U}^f, \quad \Lambda_h^f \subset \Lambda^f, \quad \mathcal{U}_h^s \subset \mathcal{U}^s \quad \text{and} \quad \Lambda_h^s \subset \Lambda^s. \tag{44}$$

Then, the discretization of the hybrid variational formulation described above is obtained in a standard way by replacing the continuous spaces in (33)-(36) by their discrete subspaces.

3. Snell's law and evanescent waves

Homogeneous free-space solutions of the partial differential equation(s) to be solved have been successfully exploited for constructing discrete spaces of the enrichment functions for acoustic scattering [2, 4–7] and elasto-dynamic [6] applications. To enable sample designs of the subspaces $\mathcal{U}_h$ (15,44), physical conditions that give rise to evanescent waves are first inspected here in more detail. In particular, the analytic form of the evanescent waves for the case of a planar interface between two semi-infinite media is derived.

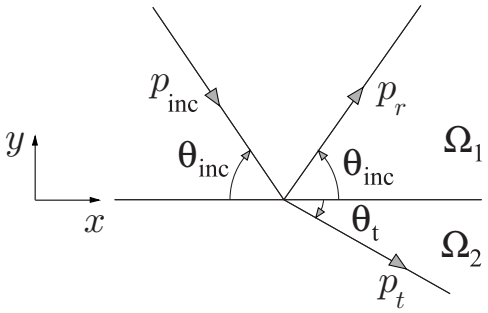

Fig. 3. Incident, reflected, and refracted waves for a wave propagation problem with a fluid/fluid interface.

3.1. Fluid/fluid interface

Consider first the case of two semi-infinite fluids separated by a planar interface as illustrated in Figure 3. When an incident wave p_{inc} passes through the interface at an oblique angle and the two fluids have different speeds of sound, it produces a reflected wave p_{r} in Ω_1 and and a refracted wave p_t in Ω_2. The relationship between the angle of the incident wave θ_{inc}, the angle of the reflected wave θ_{r}, and the speeds of sound in the two fluids, c_1 and c_2, is known as Snell's law [12]. It is sometimes also referred to as Descartes' law or the law of refraction and it is recalled below

$$\frac{\cos\theta_{\text{inc}}}{c_1} = \frac{\cos\theta_t}{c_2}. \tag{45}$$

When $c_1 < c_2$, Snell's law predicts that the angle of the refracted wave is smaller than the angle of the incident wave, i.e. $\theta_t < \theta_{\text{inc}}$. As the angle of incidence is decreased, the refracted wave eventually becomes parallel to the interface. This occurs for one particular angle of incidence, called the *critical angle*, that is given by

$$\theta_{\text{cr}} = \cos^{-1}\left(\frac{c_1}{c_2}\right), \quad \text{if} \quad c_1 < c_2. \tag{46}$$

If $\theta_{\text{inc}} < \theta_{\text{cr}}$, the refracted wave disappears, the incident wave undergoes *total internal reflection* and an *evanescent wave* occurs in the second fluid, Ω_2.

For simplicity, assume that the coordinate system is such that the interface is aligned with the x-axis, Ω_1 is the region $y > 0$, and Ω_2 is the region $y < 0$. Furthermore, assume that p_{inc}, p_r and p_t are plane waves that satisfy the Helmholtz equation (1) in their respective domains. From the transmission conditions (2) and (3), it follows that these plane waves are of the form

$$p_{\text{inc}} = A_{\text{inc}} e^{ik_1(x\cos\theta_{\text{inc}} - y\sin\theta_{\text{inc}})}, \tag{47}$$

$$p_r = A_r e^{ik_1(x\cos\theta_{\text{inc}} + y\sin\theta_{\text{inc}})}, \tag{48}$$

$$p_t = A_t e^{\beta y} e^{i\sqrt{k_2^2+\beta^2}x}, \tag{49}$$

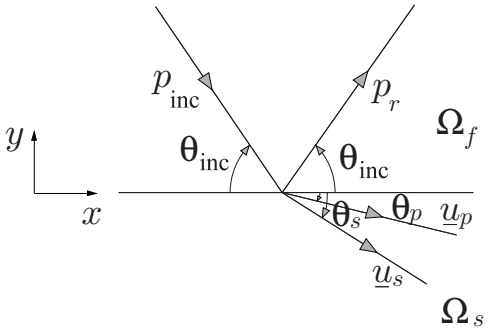

Fig. 4. Incident, reflected, and refracted waves for a wave propagation problem with a fluid/solid interface.

where $\beta = \sqrt{k_1^2 \cos^2\theta_{\text{inc}} - k_2^2}$ and the amplitudes A_{inc}, A_r and A_t are given by

$$A_r = -\frac{\rho_1\beta + ik_1\rho_2 \sin\theta_{\text{inc}}}{\rho_1\beta - ik_1\rho_2 \sin\theta_{\text{inc}}} A_{\text{inc}}, \qquad A_t = -\frac{2ik_1\rho_2 \sin\theta_{\text{inc}}}{\rho_1\beta - ik_1\rho_2 \sin\theta_{\text{inc}}} A_{\text{inc}}. \tag{50}$$

Hence β is a real number if $\theta_{\text{inc}} < \theta_{\text{cr}}$, in which case the transmitted wave p_t is evanescent and decays exponentially in the $-y$ direction. Note also that the apparent wave number of the evanescent wave p_t along the interface is $\alpha \in [k_2, k_1]$, instead of the native wave number k_2.

3.2. Fluid/solid interface

When an incident wave p_{inc} encounters a fluid solid interface, it gives rise to two transmitted waves in the solid: a pressure wave $\underline{u}_p$ and a shear wave $\underline{u}_s$, as shown in Figure 4. In this situation, Snell's law determines the relationship of the angles of propagation of these waves via

$$\frac{\cos\theta_{\text{inc}}}{c_f} = \frac{\cos\theta_p}{c_p} = \frac{\cos\theta_s}{c_s}, \tag{51}$$

where θ_{inc} is the angle of the incident wave, θ_p and θ_s are the angles of the refracted pressure and shear waves, respectively, c_f is the speed of sound in the fluid, and c_p and c_s are the elastic speeds of sound in the solid given by

$$c_p = \sqrt{\frac{\lambda_L + 2\mu_L}{\rho_s}}, \quad c_s = \sqrt{\frac{\mu_L}{\rho_s}}. \tag{52}$$

There are two critical angles: θ_{cp} for pressure waves, and θ_{cs} for shear waves. These angles are given by

$$\theta_{\text{cp}} = \cos^{-1}(\frac{c_f}{c_p}), \quad \text{if } c_f < c_p, \quad \text{and} \quad \theta_{\text{cs}} = \cos^{-1}(\frac{c_f}{c_s}), \quad \text{if } c_f < c_s. \tag{53}$$

If the interface is aligned with the x-axis, Ω_f is the region $y > 0$ and Ω_s is the region $y < 0$

and the incident, reflected and transmitted waves are in the form of plane waves, it can be shown using the transmission conditions (23) and (24) that the transmitted pressure wave $\underline{u}_p$ is evanescent if $c_f < c_p$ and $\theta_{\text{inc}} < \theta_{\text{cp}}$, the transmitted shear wave $\underline{u}_s$ is evanescent if $c_f < c_s$ and $\theta_{\text{inc}} < \theta_{\text{cs}}$, and these waves are of the form

$$p_{\text{inc}} = A_{\text{inc}} e^{ik(x\cos\theta_{\text{inc}} - y\sin\theta_{\text{inc}})}, \tag{54}$$

$$p_r = A_r e^{ik(x\cos\theta_{\text{inc}} + y\sin\theta_{\text{inc}})}, \tag{55}$$

$$\underline{u}_p = A_p \begin{bmatrix} \alpha \\ i\beta \end{bmatrix} e^{\beta y} e^{i\alpha x}, \tag{56}$$

$$\underline{u}_s = A_s \begin{bmatrix} -ib \\ a \end{bmatrix} e^{by} e^{iax}, \tag{57}$$

where

$$\alpha^2 = \beta^2 + k_p^2, \qquad \beta = \sqrt{k^2\cos^2\theta_{\text{inc}} - k_p^2}, \tag{58}$$

$$a^2 = b^2 + k_s^2, \qquad b = \sqrt{k^2\cos^2\theta_{\text{inc}} - k_s^2}, \tag{59}$$

and the amplitudes are given by

$$A_s = -\frac{2i\alpha k\sin\theta_{\text{inc}}}{\rho_f\omega^2(2\alpha a - a^2 + b^2) - i2\alpha k\sin\theta_{\text{inc}}} A_{\text{inc}}, \tag{60}$$

$$A_p = -\frac{a^2 - b^2}{2\alpha\beta} A_s, \tag{61}$$

$$A_r = -i(k_p^2\lambda_L + 2\beta^2\mu_L)A_p - 2iab\mu_L A_s - A_{\text{inc}}. \tag{62}$$

Hence, the evanescent waves $\underline{u}_p$ and $\underline{u}_s$ decay exponentially in the $-y$ direction.

4. New family of DGM elements for multiscale wave propagation problems

In general, DEM [1–7] seeks an approximate solution of its hybrid variational problem in the form of a locally enriched (low-order) polynomial. For example, in the case of Navier's elasto-dynamic equations (19), it approximates the solution $\underline{u}$ by

$$\underline{u}_h = \underline{u}_h^P + \underline{u}_h^E, \tag{63}$$

where $\underline{u}_h^P \in \mathcal{U}_h^P$ is based on the classical (low-order) finite element polynomials which are suitable for representing the large scales of the solution [3], and $\underline{u}_h^E \in \mathcal{U}_h^E$ denotes the enrichment that should be suitable for representing its small scales [3], so that

$$\mathcal{U}_h = \mathcal{U}_h^P \oplus \mathcal{U}_h^E. \tag{64}$$

More specifically, DEM constructs the enrichment field from the free-space solutions of the homogeneous part of the governing partial differential equations that are not contained in $\mathcal{U}_h^P$.

For a large class of Helmholtz problems such as acoustic scattering, the exact solution can be well represented using only the free-space solutions. For such problems, DEM drops the polynomial field from the numerical approximation, in which case the enriched elements are labeled DGM elements instead of DEM elements. On the other hand, the exact solution of an elasto-dynamic problem can contain non-oscillatory or slowly oscillatory components in space due to a specific type of loading. For this reason, DEM maintains the polynomial field in the numerical approximation when applied to the solution of some elasto-dynamic problems and the enriched elements are labeled in this case DEM elements and not DGM elements.

A family of two-dimensional, quadrilateral, DEM/DGM elements with an increasing number of plane waves and Lagrange multiplier degrees of freedom (Q-4-1, Q-8-2, Q-16-4, and Q-32-8, etc., where X and Y in the Q-X-Y terminology refer to the number of plane wave enrichment functions per element and number of Lagrange multiplier degrees of freedom per edge, respectively) was previously constructed in [2, 4, 5] for two-dimensional acoustic scattering problems. This family of elements was extended in [7] to three dimensions. Related DEM elements also labeled Q-8-2 and Q-16-4 were developed in [6] for two-dimensional elasto-dynamic problems. Here, some of these elements are first reviewed as they are the foundation of the new two-dimensional elements proposed in this paper. Next, new elements are constructed by adding evanescent waves to the previously constructed local bases of enrichment functions. As with other DEM/DGM elements, special attention is paid to the total number of Lagrange multiplier degrees of freedom introduced on the edges of the elements, in order not to violate the inf-sup condition. To this effect, the following "limitation" criterion, which was justified in [2, 4, 5], is adopted

$$n^\lambda \leq \frac{n^E}{2}, \tag{65}$$

where n^λ denotes the total number of Lagrange multiplier degrees of freedom per edge, and n^E denotes the total number of enrichment functions per element — that is, the dimension of $\mathcal{U}_h^E$.

4.1. DGM elements Q-8-2 and Q-16-4 for Helmholtz problems

The DGM element Q-8-2 is a quadrilateral element with eight plane waves and two Lagrange multipliers per edge. The DGM element Q-16-4 uses 16 plane waves and four Lagrange multipliers per edge. Higher-order DGM elements for Helmholtz problems — that is, DGM elements with more than 8 and sixteen plane waves — have also been developed (for example, see [4]) but are not specifically discussed in this paper. However, the methodology presented here is equally applicable to these elements.

By default, the plane waves in a DGM element for Helmholtz applications propagate in directions uniformly distributed around the unit circle. The enrichment space $\mathcal{U}_h^E$ for both elements Q-8-2 and Q-16-4 can be written concisely as

$$\mathcal{U}_h^E = \left\{ p_h^{PW} \in L^2(\Omega) : p_h^{PW}\Big|_\tau(\underline{x}) = \sum_{l=1}^{n^E} p_l e^{ik\underline{\theta}_l\cdot\underline{x}}, \underline{\theta}_j = [\cos\theta_j, \sin\theta_j]^T, \theta_j = \frac{2j\pi}{n^P}, j = 1, ..., n^P \right\}. \tag{66}$$

Here, the superscript PW highlights the plane wave aspect of the approximation function and the number of plane waves n^E sets the dimension of $\mathcal{U}_h^E$ in each element. By definition, $n^E = 8$ for the element Q-8-2 and $n^E = 16$ for the element Q-16-4. The coefficients p_l are the primal degrees of freedom in element τ.

It was shown in [2] that the exact solution of the one-domain version of the hybrid variational problem (8–10) satisfies

$$\lambda = \frac{\partial p}{\partial \underline{n}}, \qquad \text{on } \partial\tau_j \bigcap \partial\tau_l. \tag{67}$$

This suggested choosing λ_h as a good approximation of $\partial p_h/\partial\underline{n}$ and led to the following space of approximation of the Lagrange multiplier field

$$\Lambda_h = \left\{ \lambda_h^{PW} \in \Lambda^f : \lambda_h^{PW}\Big|_{\partial\tau\bigcap\partial\tau'}(s) = \sum_{j=1}^{n^\lambda} \lambda_j e^{ik_m s\eta_j} \right\}, \tag{68}$$

where τ and τ' are two neighboring elements, and n^λ sets the dimension of Λ_h for each edge, with $n^\lambda = 2$ for the element Q-8-2 and $n^\lambda = 4$ for the element Q-16-4. The parameter s is the abscissae along the edge $\partial\tau\bigcap\partial\tau'$ and the parameters η_j are given by [1–5]

$$\eta_1 = \frac{1}{2}, \;\; \eta_2 = -\frac{1}{2}, \qquad \text{for Q-8-2,} \tag{69}$$

$$\eta_1 = \frac{1}{5}, \;\; \eta_2 = -\frac{1}{5}, \;\; \eta_3 = \frac{3}{4}, \;\; \eta_4 = -\frac{3}{4}, \quad \text{for Q-16-4.} \tag{70}$$

4.2. DEM elements Q-8-2 and Q-16-4 for elasto-dynamic problems

The enrichment space of the quadrilateral DEM elements Q-8-2 and Q-16-4 for elastic wave propagation problems is also based on uniformly distributed planar waves. However, two types of waves occur in an elastic medium: pressure waves and shear waves [6]. For this reason, the enrichment space is constructed as follows

$$\mathcal{U}_h^{s^E} = \left\{ \underline{u}_h^{PW} \in \left(L^2(\Omega)\right)^2 : \underline{u}_h^{PW}\Big|_\tau(\underline{x}) = \sum_{j=1}^{n^E/2} u_j^p \underline{p}_j e^{ik_p \underline{p}_j\cdot\underline{x}} + \sum_{j=1}^{n^E/2} u_j^s \underline{s}_j e^{ik_s \underline{p}_j\cdot\underline{x}} \right\}. \tag{71}$$

Here, $(n^E/2) = 8$ for the element Q-8-2 and $(n^E/2) = 16$ for the element Q-16-4, u_j^p and u_j^s are the enrichment primal degrees of freedom of element τ, and $\underline{p}_j$ and $\underline{s}_j$ are the normalized

j-th pressure and shear amplitude vectors, respectively, and are given by

$$\underline{p}_j = [\cos\theta_j, \sin\theta_j]^T, \quad \underline{s}_j = [-\sin\theta_j, \cos\theta_j]^T, \quad j = 1, 2, ..., n^E/2. \tag{72}$$

The elastic wave numbers k_p and k_s can be expressed in terms of Lamé constants and the circular frequency ω as follows

$$k_p = \omega\sqrt{\frac{\rho_s}{\lambda_L + 2\mu_L}} \quad \text{and} \quad k_s = \omega\sqrt{\frac{\rho_s}{\mu_L}}. \tag{73}$$

The approximation space of the Lagrange multiplier field corresponding to the the choice of $\mathcal{U}_h^{s^E}$ expressed in (71) is based on the tractions associated with the enrichment pressure and shear waves and is given by

$$\Lambda_h^s = \left\{ \underline{\lambda}_h^{PW} \in \Lambda^s : \underline{\lambda}_h^{PW}\Big|_{\partial\tau \bigcap \partial\tau'}(s) = \sum_{j=1}^{n^\lambda} \lambda_j^p \underline{d}_j^p e^{ik_p s\eta_j^p} + \sum_{j=1}^{n^\lambda} \lambda_j^s \underline{d}_j^s e^{ik_s s\eta_j^s} \right\}, \tag{74}$$

where $n^\lambda = 2$ for the element Q-8-2, $n^\lambda = 4$ for the element Q-16-4 and λ_j^p and λ_j^s are the dual degrees of freedom on the edge $\partial\tau \bigcap \partial\tau'$. The reader is referred to [6] for the lengthy formulas defining the vector coefficients $\underline{d}_j^p$ and $\underline{d}_j^s$, and the parameters η_j^p and η_j^s.

4.3. Established performance

The performance of the quadrilateral DEM/DGM elements Q-8-2 and Q-16-4 was studied in [1–6] for various wave guide, acoustic scattering, and elastic wave propagation problems. The superiority of DEM/DGM over the classical finite element method (FEM), including the p-type FEM, was demonstrated. For example, the three-dimensional extensions of the DGM elements reviewed above were shown in [7] to reduce by one to two orders of magnitude the CPU time required by the p-type FEM for the solution of several three-dimensional wave guide and acoustic scattering problems in the medium frequency regime.

Wave propagation problems with fluid/fluid, fluid/solid, or solid/solid interfaces give rise however to multiscale wave propagation problems with evanescent waves that have different scales and characteristics than the traveling waves on which the basic DGM elements are based on. For this reason, the DEM/DGM elements Q-8-2 and Q-16-4 reviewed above are further enriched in the following sections to improve their efficiency when applied to the solution of wave propagation problems with evanescent waves. The resulting elements are labeled Q-8-2* and Q-16-4*, respectively.

4.4. DGM elements Q-8-2 and Q-16-4* for problems with fluid/fluid interfaces*

To keep the notation as simple as possible, the fluid/fluid interface is assumed to be aligned with the x-axis and the local coordinates are set up in such a way that the negative y direction points into the subdomain Ω_2. An evanescent wave occurs there if $c_1 < c_2$ and $\theta_{\text{inc}} < \theta_{\text{cr}}$.

The DGM element Q-8-2* is constructed by further enriching the DGM element Q-8-2 with evanescent waves. More specifically, the plane wave approximation of the solution and its corresponding Lagrange multiplier field are re-written, element by element and edge by edge, as

$$p_h^E(\underline{x}) = p_h^{PW}(\underline{x}) + p_h^{EW}(\underline{x}), \quad \text{and} \quad \lambda_h(s) = \lambda_h^{PW}(s) + \lambda_h^{EW}(s), \tag{75}$$

where the element indices have been dropped to simplify the notation. As before, $p_h^{PW}(\underline{x})$ combines in this case eight plane waves

$$p_h^{PW}(\underline{x}) = \sum_{j=1}^{8} p_j^{PW} e^{ik_2 \underline{\theta}_j \cdot \underline{x}}. \tag{76}$$

On the other hand, $p_h^{EW}(\underline{x})$ is chosen here as the superposition of two evanescent waves $\Big($see Eq. (49)$\Big)$ that propagate along the fluid/fluid interface in both the positive and the negative x directions

$$p_h^{EW}(\underline{x}) = p_1^{EW} e^{\beta y} e^{i\alpha x} + p_2^{EW} e^{\beta y} e^{-i\alpha x}, \tag{77}$$

where α and β are given by

$$\alpha = k_1 \cos\theta^{EW}, \qquad \beta = \sqrt{k_1^2 \cos^2\theta^{EW} - k_2^2}, \tag{78}$$

and θ^{EW} is the angle of the incident wave giving rise to the evanescent wave $e^{\beta y} e^{i\alpha x}$. It is noted that enriching the plane wave approximation with two and only two evanescent wave functions is only one among several possible choices. Each choice leads to a different "element" with perhaps a different computational efficiency.

Also as before, λ_h^{PW} is chosen as the approximation of $\partial p_h^{PW}/\partial \underline{n}$ described in the expression (68) — that is,

$$\lambda_h^{PW}(s) = \lambda_1^{PW} e^{ik_2 s/2} + \lambda_2^{PW} e^{-ik_2 s/2}. \tag{79}$$

Following the same approach adopted for the design of λ_h^{PW}, the Lagrange multiplier field λ_h^{EW} is chosen as the following approximation of $\partial p_h^{EW}/\partial \underline{n}$

$$\lambda_h^{EW} = \begin{cases} \lambda_1^{EW} e^{i\alpha x} + \lambda_2^{EW} e^{-i\alpha x}, & \text{on horizontal edges,} \\ \lambda_1^{EW} e^{\beta y}, & \text{on vertical edges.} \end{cases} \tag{80}$$

Note that only one additional Lagrange multiplier degree of freedom is introduced on each vertical edge because the normal derivatives of the evanescent waves propagating along the

interface in opposite directions and evaluated on a vertical edge generate the same functions in y.

Eqs. (75–80) complete the definition of the quadrilateral DGM element Q-8-2* for wave propagation problems with fluid/fluid interfaces. This element has $n^E = 10$ enrichment shape functions, $n^\lambda = 4$ and $n^\lambda = 3$ Lagrange multiplier degrees of freedom on the horizontal and vertical edges, respectively, and therefore satisfies the limitation criterion (65). It is illustrated in Figure 5.

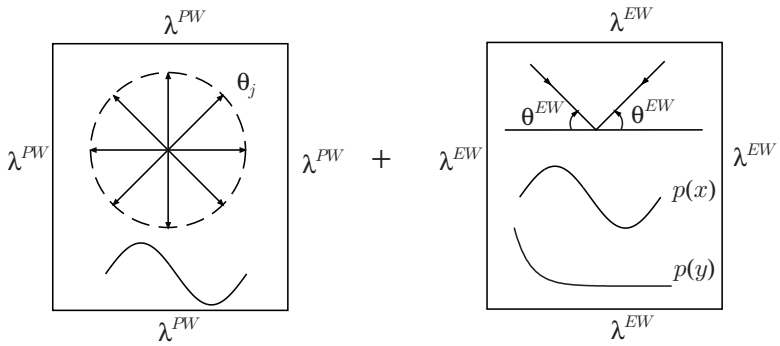

Fig. 5. DGM element Q-8-2* for wave propagation problems with fluid/fluid interfaces: superposition of eight plane waves and two evanescent waves.

The quadrilateral DGM element Q-16-4* is obtained by further enriching the DGM element Q-16-4 following the same procedure described above. More specifically, the solution is approximated by the expanded enrichment function

$$p_h^E(\underline{x}) = \sum_{j=1}^{16} p_j^{PW} e^{ik_2 \underline{\theta}_j \cdot \underline{x}} + p_h^{EW}(\underline{x}), \tag{81}$$

and its corresponding Lagrange multiplier field is refined as follows

$$\lambda_h(s) = \lambda_1^{PW} e^{ik_2 s/5} + \lambda_2^{PW} e^{-ik_2 s/5} + \lambda_3^{PW} e^{ik_2 3s/4} + \lambda_4^{PW} e^{-ik_2 3s/4} + \lambda_h^{EW}(s), \tag{82}$$

where $p_h^{EW}(\underline{x})$ and $\lambda_h^{EW}(s)$ are given by Eq. (77) and Eq. (80), respectively. Hence, the resulting DGM element Q-16-4* for wave propagation problems with fluid/fluid interfaces has $n^E = 18$ enrichment functions, $n^\lambda = 6$ and $n^\lambda = 5$ Lagrange multiplier degrees of freedom on the horizontal and vertical edges, respectively, and therefore satisfies the limitation criterion (65). It is graphically depicted in Figure 6.

4.5. DGM elements Q-8-2 and Q-16-4* for problems with fluid/solid interfaces*

Evanescent waves can also potentially arise along a fluid/solid interface, on either side of the interface, depending on the material properties. If the evanescent waves occur in the fluid along the fluid/solid interface, they can be captured by the elements described in the previous section with the wave number k_1 in the fluid replaced by the pressure wave number

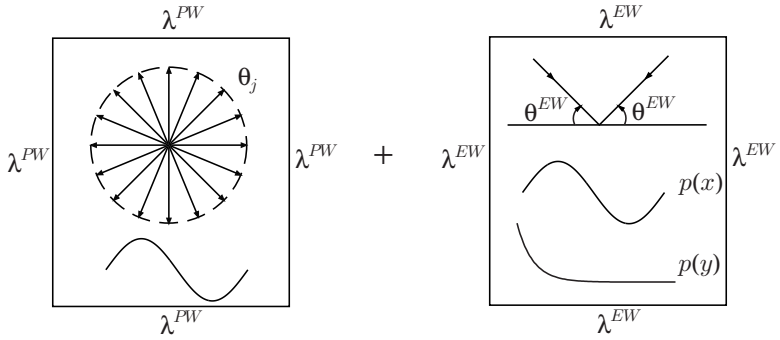

Fig. 6. DEM element Q-16-4* for problems with fluid/fluid interfaces: superposition of 16 plane waves and two evanescent waves.

k_p and/or the shear wave number k_s of the solid. However, evanescent waves occur more commonly in the solid medium. Therefore, the new DEM elements are designed here with this observation in mind.

Following the same procedure outlined in Section 4.4., the approximate solution of the fluid/solid problem is enriched by

$$\underline{u}_h^E(\underline{x}) = \sum_{j=1}^{n^E/2} u_j^p \underline{p}_j e^{ik_p \underline{p}_j \cdot \underline{x}} + \sum_{j=1}^{n^E/2} u_j^s \underline{s}_j e^{ik_s \underline{p}_j \cdot \underline{x}} + \underline{u}_h^{EW}(\underline{x}), \tag{83}$$

with $(n^E/2) = 8$ for the DEM element Q-8-2*, $(n^E/2) = 16$ for the DEM element Q-16-4*, and

$$\underline{u}_h^{EW}(\underline{x}) = u_1^{EW} \begin{bmatrix} \alpha \\ i\beta \end{bmatrix} e^{\beta y} e^{i\alpha x} + u_2^{EW} \begin{bmatrix} -\alpha \\ i\beta \end{bmatrix} e^{\beta y} e^{-i\alpha x} + u_3^{EW} \begin{bmatrix} -ib \\ a \end{bmatrix} e^{by} e^{iax} + u_4^{EW} \begin{bmatrix} -ib \\ -a \end{bmatrix} e^{by} e^{-iax}, \tag{84}$$

where

$$\beta = \sqrt{k^2 \cos^2 \theta^{EW} - k_p^2}, \quad \alpha^2 = k_p^2 + \beta^2, \tag{85}$$

$$b = \sqrt{k^2 \cos^2 \theta^{EW} - k_s^2}, \quad a^2 = k_s^2 + b^2. \tag{86}$$

As in the case of a fluid/fluid interface, the Lagrange multiplier field is approximated by $\underline{\lambda}_h = \underline{\lambda}_h^{PW} + \underline{\lambda}_h^{EW}$, where $\underline{\lambda}_h^{PW}$ is chosen in the space Λ_h^s specified in the expression (74), and $\underline{\lambda}_h^{EW}$ is chosen as an approximation of the traction $\underline{\underline{\sigma}}(\underline{u}_h^{EW})\underline{n}$. More specifically, only two additional Lagrange multiplier degrees of freedom are introduced on each edge, even though four evanescent waves are added to the enrichment, in order to maintain computational efficiency. The down selection is accomplished by carefully inspecting the analytical expressions of the tractions associated with the candidate evanescent waves for enrichment and dropping those that are "close" to the Lagrange multiplier functions already represented in the basis

Λ_h^s of the DEM element Q-8-2. This leads to

$$\underline{\lambda}_h^{EW} = \begin{cases} \lambda_1^{EW} \begin{bmatrix} a^2 - b^2 \\ 2ab \end{bmatrix} e^{iax} + \lambda_2^{EW} \begin{bmatrix} a^2 - b^2 \\ -2ab \end{bmatrix} e^{-iax}, & \text{for horizontal edges,} \\ \\ \lambda_1^{EW} \begin{bmatrix} -2ab \\ a^2 - b^2 \end{bmatrix} e^{by} + \lambda_2^{EW} \begin{bmatrix} 2ab \\ a^2 - b^2 \end{bmatrix} e^{by}, & \text{for vertical edges.} \end{cases} \tag{87}$$

In summary, the quadrilateral DGM element Q-8-2* for wave propagation problems with fluid/solid interfaces has $n^E = 20$ enrichment shape functions, $n^\lambda = 6$ Lagrange multiplier degrees of freedom per edge, and therefore satisfies the limitation criterion (65). The quadrilateral DGM element Q-16-4* has $n^E = 36$ enrichment shape functions, $n^\lambda = 10$ Lagrange multiplier degrees of freedom per edge, and therefore also satisfies the limitation criterion (65). It is illustrated in Figure 7.

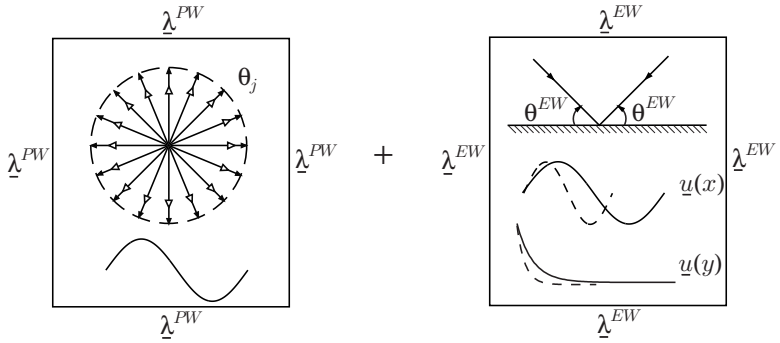

Fig. 7. DGM element Q-16-4*: superposition of 16 pressure plane waves, 16 shear plane waves, and four evanescent waves.

4.6. Remarks on extensions, robustness, and computational performance

- The discontinuous enrichment finite element concept can be viewed as a p-type finite element method in the sense that increasing the number of enrichment functions is akin to increasing the degree of a polynomial approximation. Both approaches are limited by numerical conditioning and computational complexity issues. As previously mentioned, the emphasis on the DGM elements Q-8-2 and Q-16-4 is for the sake of illustrating the rather general idea presented in this paper with sample developments. Higher-order DEM/DGM elements with even a larger number of evanescent wave enrichment functions can be constructed using the same procedure illustrated above.
- The case of a solid/solid interface can be treated by DEM following the same approach described in the previous sections for the fluid/fluid and fluid/solid interfaces. Constructing the appropriate evanescent wave enrichment functions would require however deriving first the analytic form of the evanescent waves for the case of a planar interface between two

semi-infinite solid media. This is a feasible task, but slightly more complex than that associated with a fluid/fluid or fluid/solid interface.

- Due to the decaying nature of evanescent waves, the new DEM/DGM elements may be necessary only near interfaces. This remark is explored in the next section.
- In practical DEM/DGM computations, the enrichment degrees of freedom can be condensed out at the local (element) level. Hence, the overall computational complexity of a DEM/DGM discretization is determined mostly by the number of Lagrange multiplier degrees of freedom. This has been discussed at length in the DEM/DGM references cited in the introduction of this paper.
- The local matrices associated with the various enrichment fields can be evaluated analytically on all elements with simple shapes. Indeed, because the enrichment functions are solutions of the homogeneous part of the differential equation to be solved, integration by part transforms the domain integrals associated with the mass and stiffness matrices into boundary integrals. The integrands being simple exponentials, this enables the analytical evaluation of all contributions of all enrichment fields to the mass and stiffness matrices (see [5] for two-dimensional wave propagation problems and [7] for three-dimensional ones). This is a significant advantage for DEM/DGM as many other enrichment methods require higher-order quadrature rules for evaluating the mass and stiffness matrices, thereby increasing computational complexity and reducing robustness.
- While the new elements are described here for a planar interface, they may also be applied to smooth curved interfaces by working in a local coordinate frame near the curved interface. In this case, the enrichment functions and the Lagrange multipliers described here are an approximation of the free-space solution.
- Because the exponential function $e^{\beta y}$ decays away from an interface in the direction $y < 0$, the inclusion of evanescent waves in a basis can result in nearly singular local stiffness matrices, in particular for the elements far away from an interface, where the evanescent waves as given, for example, in (77) become much smaller than the planar waves. To prevent this from happening, the evanescent enrichment functions are scaled in each element by the multiplicative constant $e^{-\beta y_0}$ so that their maximum is equal to one in the element. The same scaling technique is applied to the Lagrange multiplier approximation on each edge.

5. Performance assessment

In this section, the performance of the newly constructed DGM elements Q-8-2* and Q-16-4* is assessed on benchmark fluid/fluid and fluid/solid wave propagation problems set in the medium frequency regime. These problems have known analytic solutions that suggest and justify dropping the polynomial field from their approximation by a DEM element, which is adopted here. The performance of these new elements is compared to both the performance of the original DGM elements which do not enrich the approximation by evanescent wave functions, and to that of the standard (polynomial) Galerkin finite element method. The case of a fluid/fluid interface problem is discussed first.

5.1. Numerical results for the fluid/fluid model wave propagation problem

The square domain $\Omega = [-1,1] \times [-1,1]$ shown in Figure 8, is divided into two subdomains: $\Omega_1 = [-1,1] \times [0,1]$ which is assumed to be filled with air, and $\Omega_2 = [-1,1] \times [-1,0]$ which is assumed to be filled with water. The Robin boundary condition (4) is applied on the boundaries $\Gamma_m, \quad m = 1,2$, with $g_m = \dfrac{\partial p_m^{\text{ex}}}{\partial \underline{n}} - ik_m p_m^{\text{ex}}$, where the exact solution $p_1^{\text{ex}} = p_{\text{inc}} + p_r$ in Ω_1 and $p_2^{\text{ex}} = p_t$ in Ω_2 is shown in Figure 3. The incident wave p_{inc}, the reflected wave p_r, and the transmitted (refracted or evanescent) waves are given by Eqs. (47–50) with $\rho_1 = 1.29 kg/m^3$, $\rho_2 = 1000 kg/m^3$, and $A_{\text{inc}} = 1$. The speed of sound in air is $c_1 = 343 m/s$ and that in water is $c_2 = 1533 m/s$. Hence, the critical angle of incidence is $\theta_{\text{cr}} = 77.16^o$. The wave numbers $k_1 = \omega/c_1$ and $k_2 = \omega/c_2$, and the angle(s) of the incident wave θ_{inc} are specified later in this section.

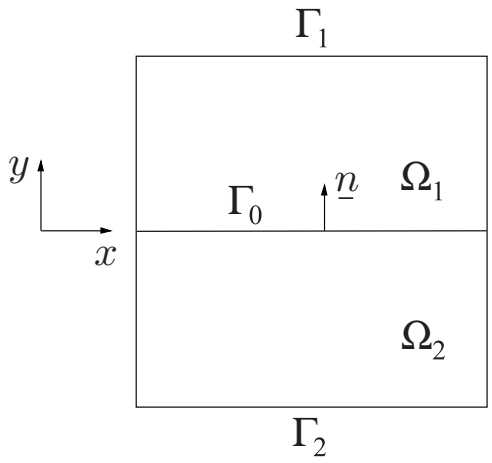

Fig. 8. Computational domain Ω for a fluid/fluid model wave propagation problem.

Since c_1 is smaller than c_2, the wave number k_1 is greater than k_2. Thus, a coarser mesh may be used in subdomain Ω_2 if a constant number of elements per wavelength is considered. As the ratio of wavelength in water and air is about four, three types of two-subdomain computational meshes are considered as shown in Figure 9: (a) a matching mesh, (b) a "coarse-2" mesh (meaning the mesh in Ω_2 is twice coarser than that in Ω_1), and (c) a "coarse-4" mesh (meaning the mesh in Ω_2 is four times coarser than that in Ω_1). The coarse-2 and coarse-4 meshes are not considered here for the standard Galerkin FEM as this would require the use of mortars or other special techniques for gluing the subdomain solutions. On the other hand, the DGM elements already incorporate Lagrange multipliers on their interfaces to enforce there a weak continuity of the solution; therefore, their usage on non-matching meshes requires no special treatment.

The discretization error is measured separately in subdomains $\Omega_m, m = 1,2$. The relative error of the classical FEM is measured by the discrete L_2 norm over all the vertices in the

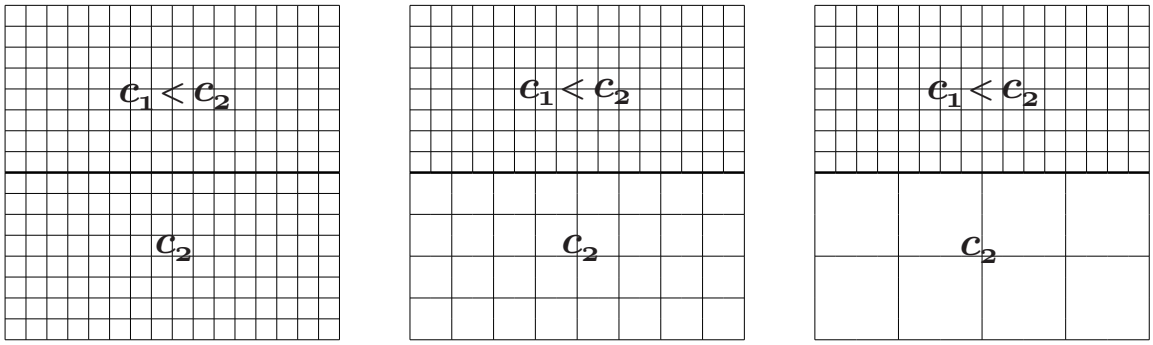

(a) (b) (c)

Fig. 9. Computational meshes: (a) matching mesh; (b) coarse-2 mesh; (c) coarse-4 mesh.

subdomains, i.e., by

$$\frac{\|p^{\mathrm{ex}} - p_h^{\mathrm{FEM}}\|_{\Omega_m}}{\|p^{\mathrm{ex}}\|_{\Omega_m}} = \frac{\sqrt{\sum\limits_{V \in \Delta^m_{\mathrm{vert}}} |(p^{\mathrm{ex}} - p_h^{\mathrm{FEM}})(V)|^2}}{\sqrt{\sum\limits_{V \in \Delta^m_{\mathrm{vert}}} p^{\mathrm{ex}}(V)^2}}, \tag{88}$$

where Δ^m_{vert} denotes the set of all the vertices in the mesh $\Delta^m_h, m = 1, 2$. The error of a DGM solution is measured using the same metric. However, since the DGM solution is discontinuous at the vertices, it is first averaged as follows

$$\tilde{p}_h^{\mathrm{DGM}}(V) = \frac{1}{n^m_{\mathrm{vert}}} \sum_{\substack{\tau \in \Delta^m_h \\ V \in \tau}} p_h^{\mathrm{DGM}}|_\tau(V), \tag{89}$$

where $n^m_{\mathrm{vert}}, m = 1, 2$, denotes the number of elements in subdomain Ω_m sharing the vertex V. Then, its relative error is computed as

$$\frac{\|p^{\mathrm{ex}} - p_h^{\mathrm{DGM}}\|_{\Omega_m}}{\|p^{\mathrm{ex}}\|_{\Omega_m}} = \frac{\sqrt{\sum\limits_{V \in \Delta^m_{\mathrm{vert}}} |(p^{\mathrm{ex}} - \tilde{p}_h^{\mathrm{DGM}})(V)|^2}}{\sqrt{\sum\limits_{V \in \Delta^m_{\mathrm{vert}}} p^{\mathrm{ex}^2}}} \tag{90}$$

The new DGM elements Q-8-2* and Q-16-4* depend on the parameter θ^{EW}. In the following computations, this parameter is set to

$$\theta^{EW} = \frac{2}{5}\theta_{\mathrm{cr}} = 30.86^o$$

based on numerical experience.

Various strategies for exploiting the new DGM elements can be developed with regard to the trade-offs between the number of degrees of freedom, approximation properties, and numerical stability. Here, the following two strategies are explored.

Strategy I (Figure 10): *The evanescent wave degrees of freedom are activated in every element*

of the subdomain Ω_2, but the corresponding Lagrange multiplier degrees of freedom are activated only on the horizontal edges in Ω_2.

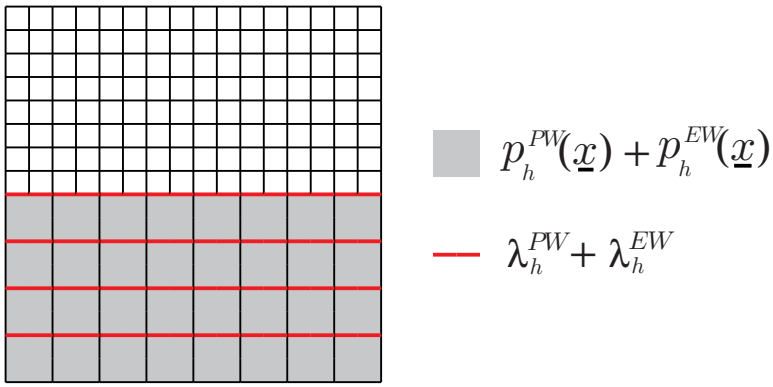

Fig. 10. Strategy I: enrichment by evanescent wave functions is applied in every element of Ω_2, but the corresponding Lagrange multiplier field is applied only on the horizontal edges in Ω_2.

Since evanescent waves decay exponentially away from the interface, adding evanescent waves into the approximation space of the elements located far away from the interface may not be necessary. Therefore, the following strategy is also considered.

Strategy II (Figure 11): *The evanescent wave degrees of freedom are activated only in the first two layers of elements starting from the layer connected to the interface in subdomain Ω_2 and the corresponding Lagrange multiplier degrees of freedom are activated on all horizontal edges of the first-layer elements.*

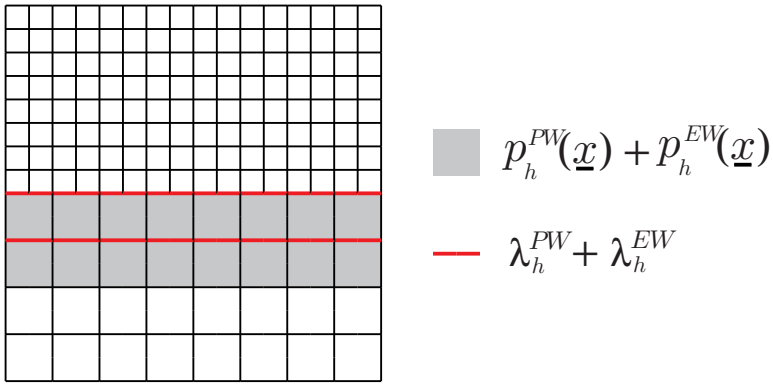

Fig. 11. Strategy II: enrichment by evanescent wave functions is applied only in the first two layers of elements starting from the layer connected to the interface in subdomain Ω_2 and the corresponding Lagrange multiplier field is introduced on all horizontal edges of first-layer elements.

In all cases, the two subdomains are uniformly discretized (see Figure 9). The mesh size is varied to perform mesh convergence studies. For DGM, the degree of freedom count is based on the total number of Lagrange multiplier degrees of freedom because the enrichment variables are condensed out at the element level. In order to perform meaningful performance comparisons, the internal degrees of freedom of the standard (higher-order) FEM elements are also condensed out at the element level and therefore are also not included in the degree of freedom count.

As mentioned earlier, the DEM/DGM can be viewed as a higher-order FEM in which the number of enrichment shape functions is increased within an element instead of the degree of an underlying polynomial. In [2], it was shown that the DGM element Q-8-2 and the standard bi-quadratic Galerkin element Q_2 have comparable convergence rates and computational complexities, but Q-8-2 has a significantly smaller error constant and therefore significantly better accuracy. Similarly, it was shown in [4] that the DGM element Q-16-4 has a convergence rate similar to that of the standard bi-quartic Galerkin element Q_4 and a comparable computational complexity, but a superior accuracy. Hence for these reasons, the comparisons performed in this paper are those between the performances of the DGM elements Q-8-2* and Q-8-2 and the standard Galerkin element Q_2 on one hand, and the DGM elements Q-16-4* and Q-16-4 and the standard Galerkin element Q_4 on the other hand.

Since in practical computations the exact solution may be a combination of plane waves and evanescent waves, the benchmark problem defined above is solved for angles of incidence varying from $\theta_{\text{inc}} = 1^o$ to 90^o in one-degree increments. For each assessed numerical solution method, the obtained numerical errors are averaged over all considered angles of incidence and the average value is graphically displayed.

Figure 12 compares the performance results of the DGM element Q-8-2* using Strategy I, the DGM element Q-8-2, and the standard Galerkin element Q_2 in the medium frequency regime $k_1 = 120$ and $k_2 = 26.67$. These results show that when computing on the matching mesh, the DGM element Q-8-2* achieves the 1% level of relative error in subdomain Ω_2 where evanescent waves occur for a subset of the considered values of the angle of incidence, using less than half the degrees of freedom required by the original DGM element Q-8-2 which itself requires less than half the degrees of freedom needed by the standard Galerkin element Q_2 for the same purpose. The advantage of the new enrichment by evanescent wave functions is even more apparent in the case of computations on the coarse-2 and coarse-4 meshes where the DGM element Q-8-2* is shown to achieve the 99% level of accuracy using about eight times fewer degrees of freedom than the original DGM element Q-8-2. The performance of the DGM elements in subdomain Ω_1 is little affected by the inclusion of evanescent waves in the enrichment field because in this case the sub-scale evanescent waves occur on the other side of the fluid/fluid interface. However even in Ω_1, the performance of the DGM elements Q-8-2* and Q-8-2 is found to be far superior to that of the standard Galerkin element Q_2.

Figure 13 reports on similar performance results as Figure 12 but using Strategy II for the DGM element Q-8-2*. The advantage of the new DGM element is even bigger in this case. This is because introducing the new enrichment by evanescent wave functions in the first two layers of elements in Ω_2 below the interface proves to be sufficient and reduces the total number of degrees of freedom associated with the discretization by the DGM element Q-8-2*. When applied on the matching mesh, Q-8-2* achieves in subdomain Ω_2 a relative error of 1% using six times fewer degrees of freedom than the bi-quadratic element Q_2. When applied on the coarse-2 and coarse-4 meshes, discretization by the DGM element Q-8-2* is shown to reduce by a factor larger than 10 the number of degrees of freedom required by Q-8-2 for reaching this level of accuracy in subdomain Ω_2.

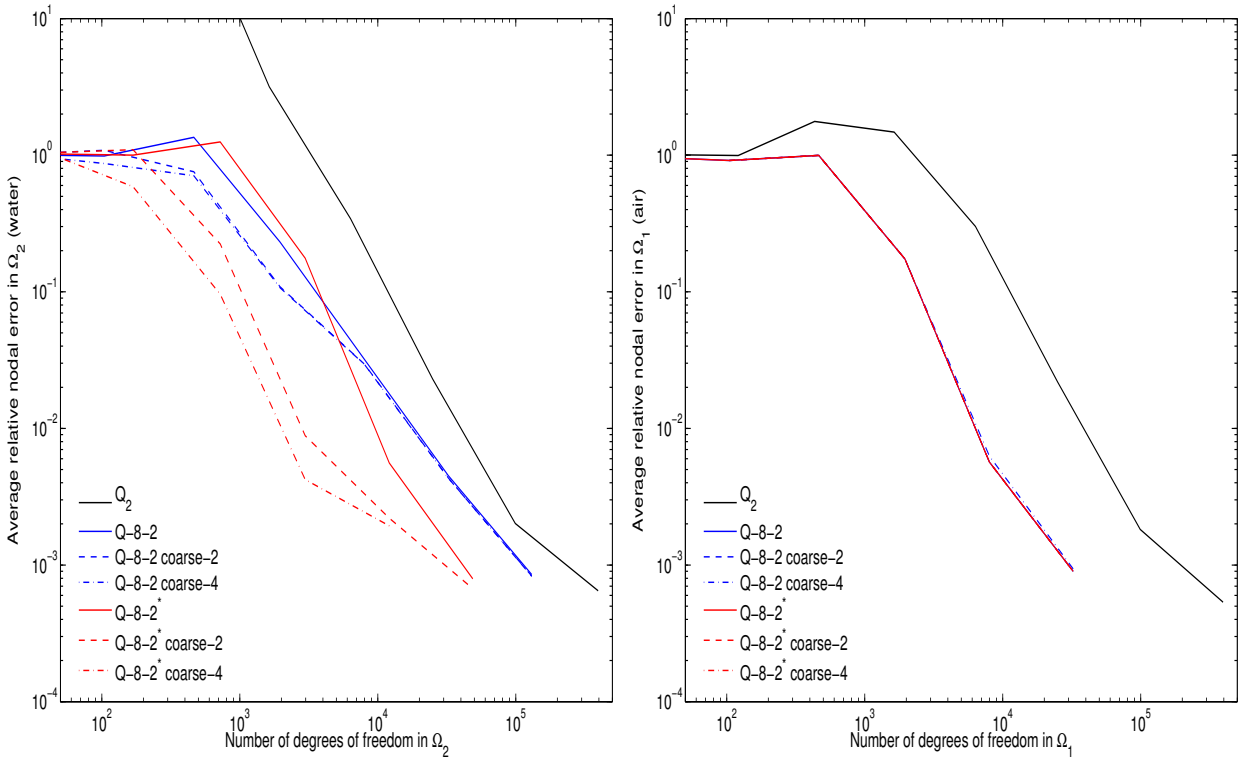

Fig. 12. Fluid/fluid model wave propagation problem: performance comparison of Q-8-2* (Strategy I), Q-8-2 and Q_2 in Ω_2 (left) and Ω_1 (right) for $k_1 = 120$ and $k_2 = 26.67$. The plotted error is the average of the relative errors obtained for $1^o \leq \theta_{\text{inc}} \leq 90^o$.

Figure 14 summarizes the performance results obtained for the particular case where $\theta_{\text{inc}} = 20^o$, which is well below the critical angle $\theta_{\text{cr}} = 77.16^o$. The same trends are observed as when averaging over all considered incident waves. However in this particular case, the advantage of enrichment with evanescent wave functions is well demonstrated even on the matching mesh.

Next, the wave numbers are increased to $k_1 = 320$ and $k_2 = 80$. For this higher frequency regime, the higher-order elements Q-16-4*, Q-16-4, and Q_4 are more appropriate and are therefore considered. In view of the superior performance results achieved by the DGM element Q-8-2* using Strategy II, this strategy is adopted for Q-16-4*. Figure 15 summarizes the obtained performance results. Again, the plotted error is the average of the relative errors obtained when the incident angle is varied between $\theta_{\text{inc}} = 1^o$ and 90^o by increments of 1^o. The new DGM element Q-16-4* exhibits a better performance than the DGM element Q-16-4 in Ω_2 for all considered meshes. In particular, when computing on the coarse-2 and coarse-4 meshes, the accuracy level achieved in subdomain Ω_2 by the DGM element Q-16-4* is an order of magnitude higher than that achieved by the original DGM element Q-16-4. The performance improvement of Q-16-4* over Q-16-4 is however a little smaller than that of Q-8-2* over Q-8-2, which suggests that enriching Q-16-4 with more than two evanescent wave functions would be beneficial. Note also that for high levels of accuracy, some performance improvement due to enrichment by evanescent wave functions is noticeable on the coarser meshes even in subdomain Ω_1. Finally, the reader can also observe that at the considered

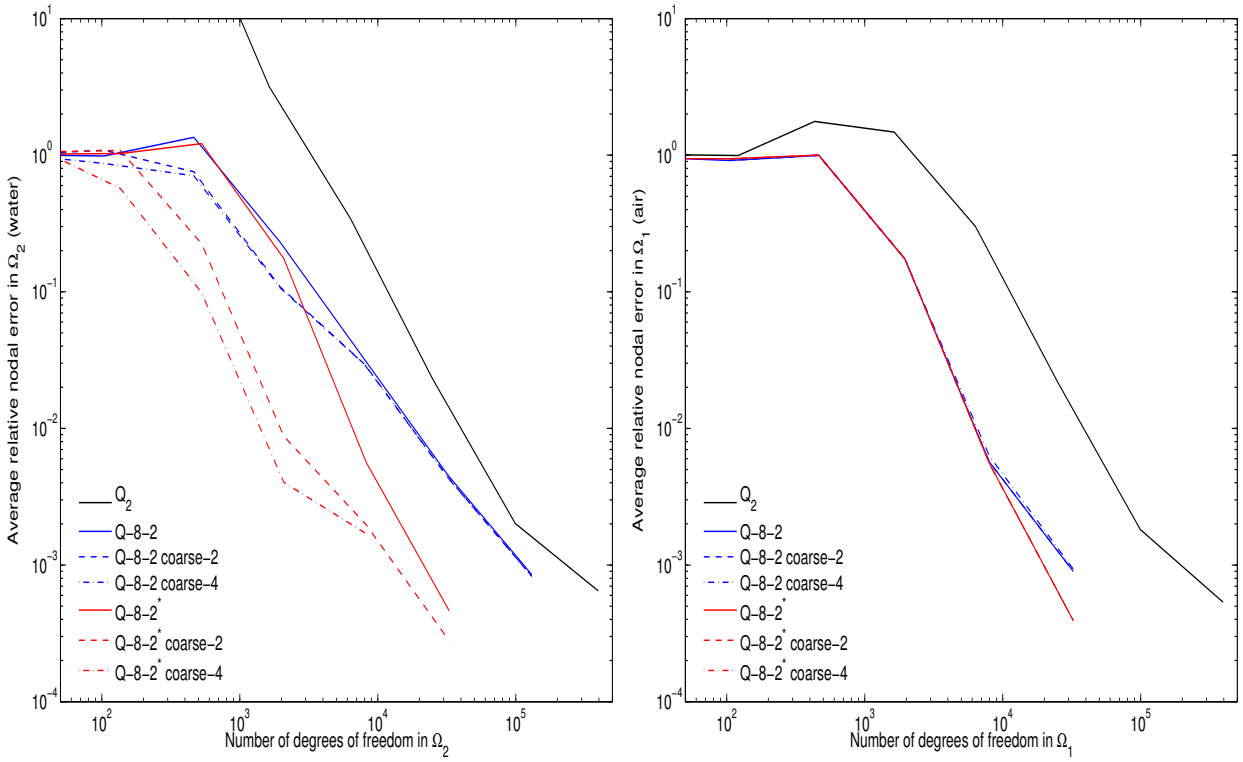

Fig. 13. Fluid/fluid model wave propagation problem: performance comparison of Q-8-2* (Strategy II), Q-8-2 and Q_2 in Ω_2 (left) and Ω_1 (right) for $k_1 = 120$ and $k_2 = 26.67$. The plotted error is the average of the relative errors obtained for $1^o \leq \theta_{\text{inc}} \leq 90^o$.

higher frequency regime, both DGM elements Q-16-4* and Q-16-4 outperform the standard higher-order element Q_4 by a significant margin. For example on a matching mesh, the element Q-16-4* reaches the relative error 10^{-3} in both subdomains Ω_1 and Ω_2 using eight to nine times fewer degrees of freedom than the standard higher-order element Q_4.

5.2. Numerical results for the fluid/solid model wave propagation problem

Here, the considered problem is governed by the boundary value problem (21-26) and defined in the square domain $\Omega = [-1, 1] \times [-1, 1]$ shown in Figure 16. The upper half subdomain Ω_f is filled with water and the lower half subdomain Ω_s is made of steel characterized by the Lamé constants $\lambda_L = 9.24e + 10$ and $\mu_L = 7.87e + 10$. The Robin boundary condition (26) is imposed on the boundary Γ_f with $g_f = \dfrac{\partial p^{\text{ex}}}{\partial \underline{n}} - ikp^{\text{ex}}$, where $p^{\text{ex}} = p_{\text{inc}} + p_r$ is the exact pressure solution in Ω_f. The natural boundary condition (25) with $\underline{g}_s = \underline{\underline{\sigma}}(\underline{u}^{\text{ex}})\underline{n}$ is imposed on the boundary Γ_s, where the exact solution for the displacement field in Ω_s is $\underline{u}^{\text{ex}} = \underline{u}_p + \underline{u}_s$ and is shown in Figure 4. The incident wave p_{inc}, the reflected wave p_r, and the transmitted waves $\underline{u}_p$ and $\underline{u}_s$ are given in Eqs. (54-62).

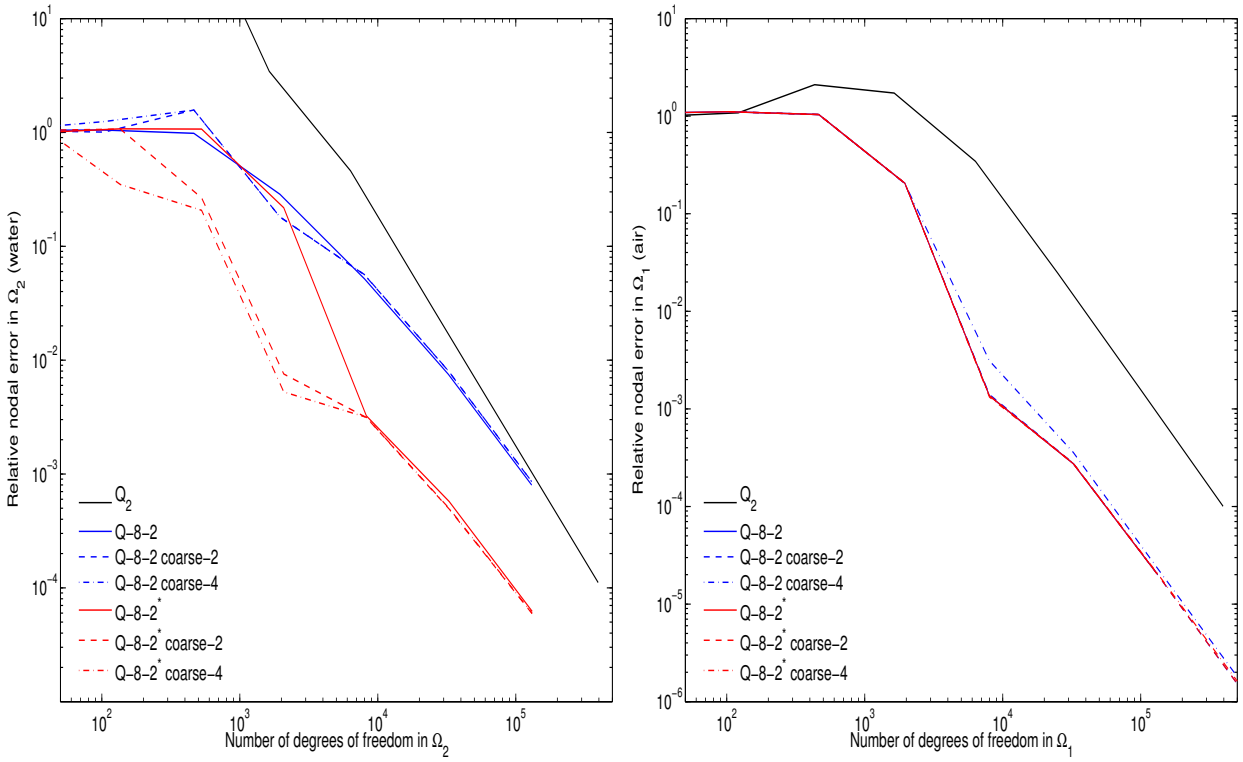

Fig. 14. Fluid/fluid model wave propagation problem: performance comparison of Q-8-2* (Strategy II), Q-8-2 and Q_2 in Ω_2 (left) and Ω_1 (right) for $k_1 = 120$, $k_2 = 26.67$, and $\theta_{\text{inc}} = 20^o$.

The critical angles for the pressure and shear waves are

$$\theta_{\text{cs}} = 61.87^o, \qquad \theta_{\text{cp}} = 74.66^o. \tag{91}$$

The parameter θ^{EW} used in the construction of new DGM elements is set to

$$\theta^{EW} = \frac{2}{5}\theta_{\text{cs}} = 24.75^o.$$

As for the case of the fluid/fluid model wave propagation problem, uniform matching, coarse-2, and coarse-4 meshes are considered. The new DGM elements are applied with the following computational strategy, which is a variant of Strategy II defined in the previous section.

Strategy II' (Figure 17): *The evanescent wave degrees of freedom are activated only in the elements connected to the interface in subdomain Ω_s and the corresponding Lagrange multiplier degrees of freedom are activated at all the inner edges of these elements with the exception of the interface edges.*

Again, the discretization error is measured separately in the fluid and solid subdomains Ω_f and Ω_s. In the fluid subdomain Ω_f, the relative errors are computed using Eqs. (88-89) after replacing Ω_m by the fluid subdomain Ω_f. In the solid subdomain Ω_s, the relative errors are

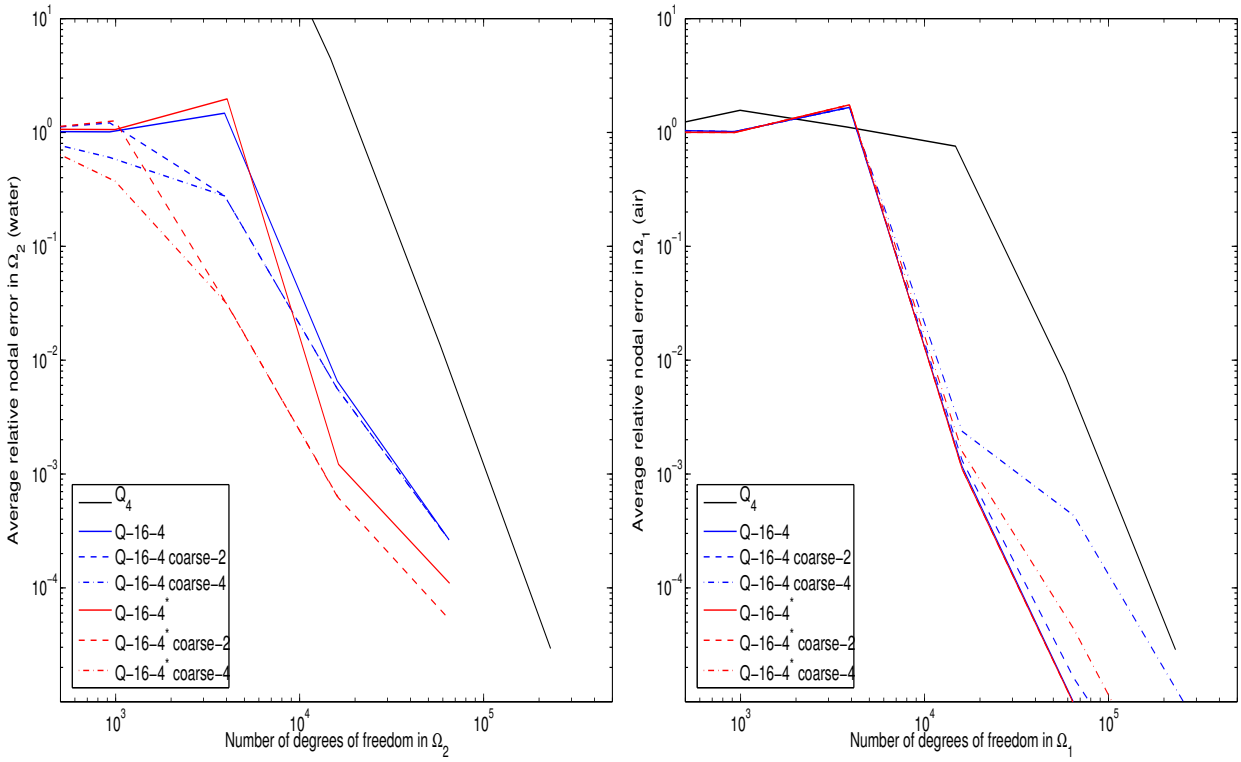

Fig. 15. Fluid/fluid model wave propagation problem: performance comparison of Q-16-4* (Strategy II), Q-16-4 and Q_4 in Ω_2 (left) and Ω_1 (right) for $k_1 = 360$ and $k_2 = 80$. The plotted error is the average of the relative errors obtained for $1^o \leq \theta_{\text{inc}} \leq 90^o$.

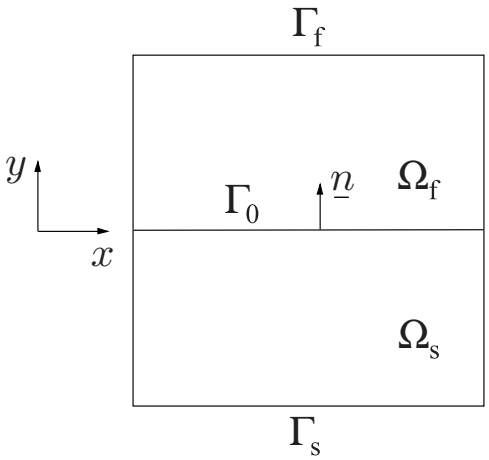

Fig. 16. Computational domain Ω for a fluid/solid model wave propagation problem.

computed in a similar fashion as follows

$$\frac{\|\underline{u}^{\text{ex}} - \underline{u}_h^{\text{FEM}}\|_{\Omega_s}}{\|\underline{u}^{\text{ex}}\|_{\Omega_s}} = \frac{\sqrt{\sum_{V \in \Delta_{\text{vert}}^s} \|(\underline{u}^{\text{ex}} - \underline{u}_h^{\text{FEM}})(V)\|^2}}{\sqrt{\sum_{V \in \Delta_{\text{vert}}^s} \|\underline{u}^{\text{ex}}(V)\|^2}}, \tag{92}$$

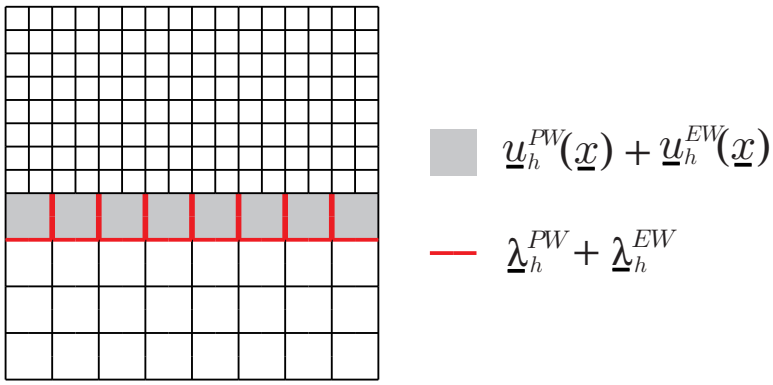

Fig. 17. Strategy II': enrichment by evanescent wave functions is applied only in the elements connected to the interface in subdomain Ω_s and the corresponding Lagrange multiplier field is introduced on all the inner edges of these elements, except for the interface edges.

where Δ^s_{vert} denotes the set of all the vertices in the mesh Δ^s_h, and

$$\frac{\|\underline{u}^{\text{ex}} - \underline{u}_h^{\text{DGM}}\|_{\Omega_s}}{\|\underline{u}^{\text{ex}}\|_{\Omega_s}} = \frac{\sqrt{\sum\limits_{V \in \Delta^s_{\text{vert}}} \|(\underline{u}^{\text{ex}} - \tilde{\underline{u}}_h^{\text{DGM}})(V)\|^2}}{\sqrt{\sum\limits_{V \in \Delta^s_{\text{vert}}} \|\underline{u}^{\text{ex}}(V)\|^2}}, \tag{93}$$

where $\tilde{\underline{u}}_h^{\text{DGM}}(V)$ is given by

$$\tilde{\underline{u}}_h^{\text{DGM}}(V) = \frac{1}{n^s_{\text{vert}}} \sum_{\substack{\tau \in \Delta^s_h \\ V \in \tau}} \underline{u}_h^{\text{DGM}}|_\tau(V), \tag{94}$$

and n^s_{vert} denotes the number of elements in subdomain Ω_s sharing the vertex V.

First, the angle of incidence is set to $\theta_{\text{inc}} = 30^o$. From Eqs. (91), it follows that $\theta_{\text{inc}} < \theta_{\text{cs}} < \theta_{\text{cp}}$ and therefore the exact solution in the solid subdomain is in this case a combination of an evanescent pressure wave and an evanescent shear wave. Figure 18 reports the performance results obtained for the DGM elements Q-8-2* and Q-8-2 and the standard Galerkin element Q_2 in the medium frequency regime defined by $k = 40$, $k_p = 10.58$ and $k_s = 18.86$. It is observed that Q-8-2* delivers an accuracy improvement over Q-8-2 for all three meshes. For a given number of degrees of freedom, the DGM element Q-8-2* reduces the error in the solid subdomain associated with the element Q-8-2 by almost an order of magnitude. When computing on the coarse meshes, Q-8-2* reduces significantly the error of the numerical solution obtained with Q-8-2 even in the fluid subdomain.

Next, the angle of incidence is varied between 1^o and 90^o in one degree increments. In this case, all reported errors correspond to the averages of the relative errors obtained for all considered values of the angle of incidence. Figure 19 shows that in this case, Q-8-2* delivers performance improvements over Q-8-2 that are similar to those delivered in the case of $\theta_{\text{inc}} = 30^o$. In particular, the discretization by the DGM element Q-8-2* is found to reach the 99% level of accuracy in the solid subdomain where evanescent waves can occur using five times fewer degrees of freedom than that by the DGM element Q-8-2 when using the

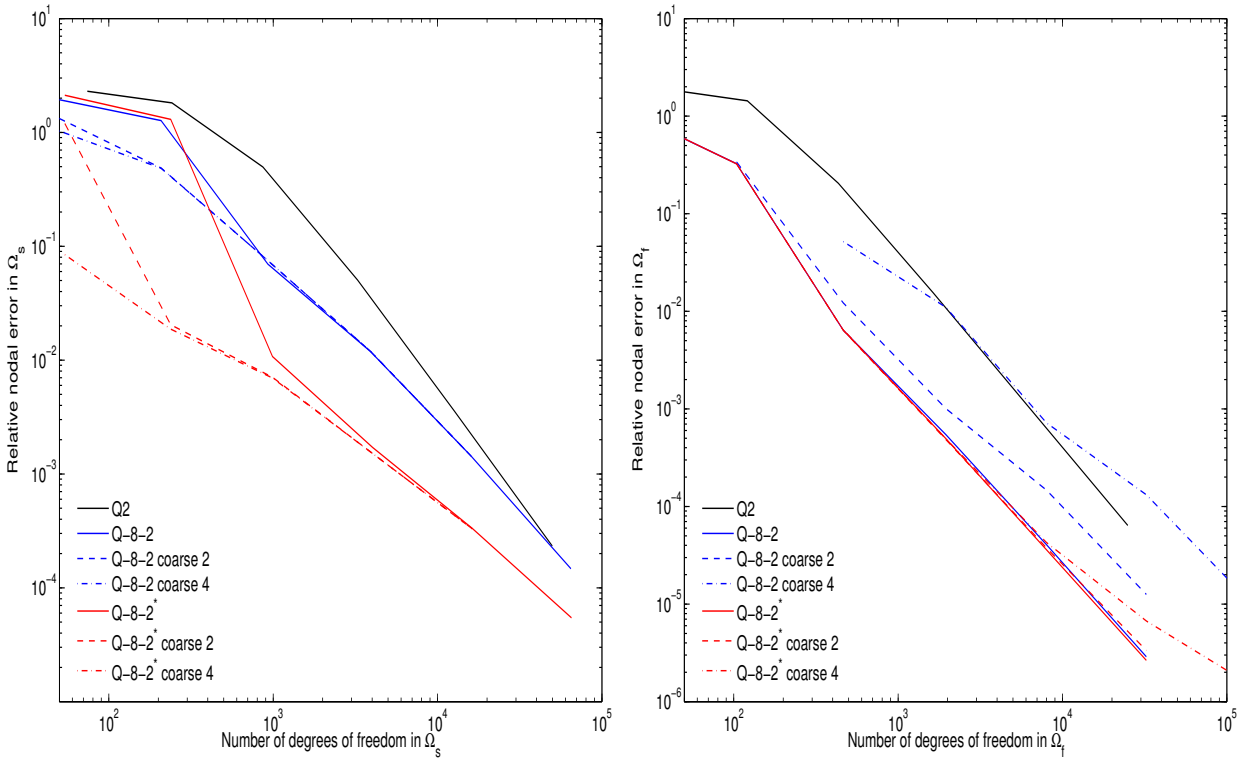

Fig. 18. Fluid/solid model wave propagation problem: performance comparison of Q-8-2*, Q-8-2, and Q_2 in Ω_s (left) and Ω_f (right) for $k = 40$, $k_p = 10.58$, $k_s = 18.86$, and $\theta_{\text{inc}} = 30^o$.

coarse-2 and coarse-4 meshes.

Finally, the wave numbers are increased to $k = 160$, $k_p = 42.34$ and $k_s = 75.43$, and attention is focused on the performance of the higher-order elements Q-16-4*, Q-16-4, and Q_4. Figure 20 shows that using the coarse meshes, discretization by the DGM element Q-16-4* reaches the 98% level of accuracy in the solid subdomain using approximately five times fewer degrees of freedom than that by the Q-16-4 element. Using the matching mesh, the new element delivers this accuracy with about five times fewer degrees of freedom than the discretization by the fourth-order polynomial element Q_4. Because of the high convergence rates of these elements, the differences in the accuracy they deliver for a fixed number of degrees of freedom is even more striking. When computing on the coarse meshes, Q-16-4* is found to deliver considerable performance improvements over Q-16-4 in the fluid subdomain, as a result of the accuracy improvement of the discretization in the solid subdomain.

6. Conclusions

Evanescent waves occur in layered media when the angle of incidence of a wave impinging on an interface is below a critical value. When the different media are characterized by sufficiently different speeds of sound, the solution of the resulting wave propagation problem exhibits multiscale components and features that are difficult to capture numerically

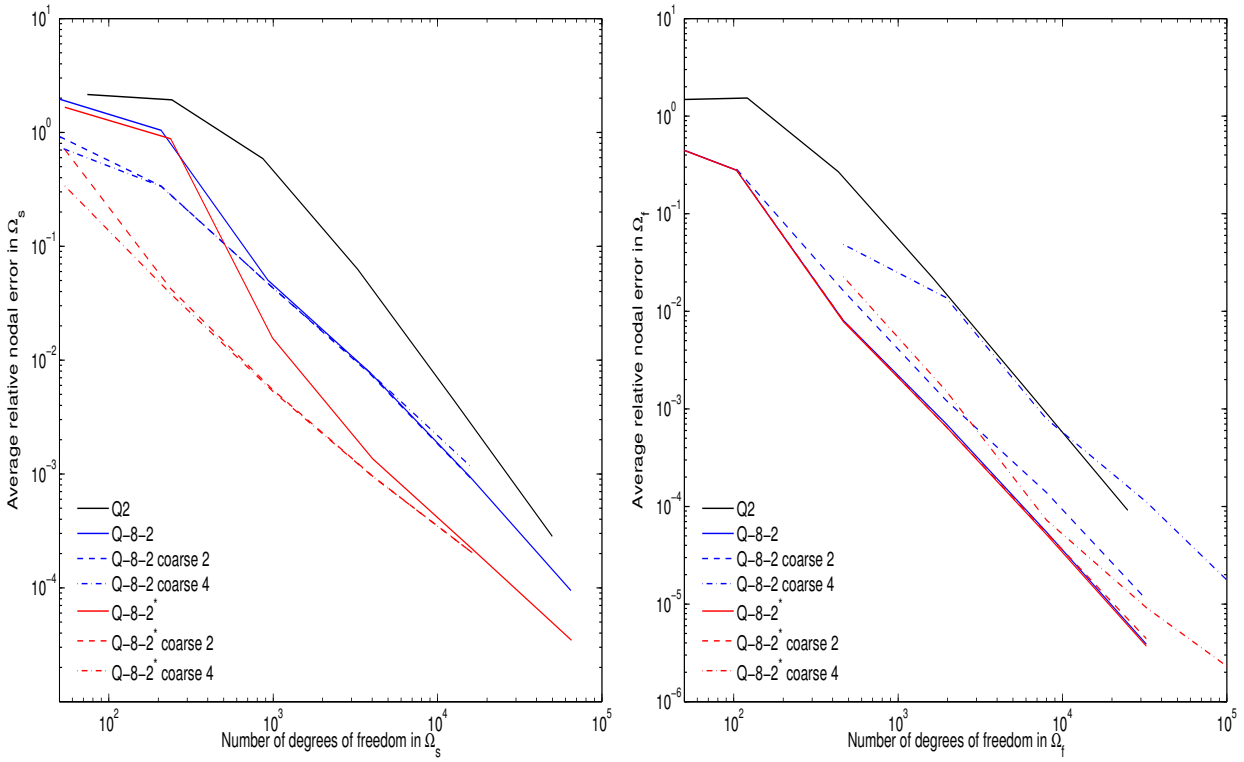

Fig. 19. Fluid/solid model wave propagation problem: performance comparison of Q-8-2*, Q-8-2, and Q_2 in Ω_s (left) and Ω_f (right) for $k = 40$, $k_p = 10.58$, and $k_s = 18.86$. The plotted error is the average of the relative errors obtained for $1^o \leq \theta_{\text{inc}} \leq 90^o$.

by standard approximation methods. On the other hand, enrichment-based discretization approaches such as the Discontinuous Enrichment Method (DEM) and its variant known as the Discontinuous Galerkin Method (DGM) with plane waves and Lagrange multipliers can be well-suited for solving such problems. In this paper, it is shown that further enriching the DGM elements previously developed for the solution of wave propagation problems in the medium frequency regime with evanescent wave functions derived analytically for a planar interface between two semi-infinite media leads to an effective multiscale solution method. Indeed, numerical tests on two-dimensional fluid/fluid and fluid/solid model wave propagation problems reveal that the new DGM elements combining plane wave and evanescent wave shape functions can reduce the number of degrees of freedom required by the DGM elements with plane wave shape functions only and the standard higher-order polynomial finite elements by up to almost an order of magnitude. Furthermore, the new DGM elements can be applied locally as necessary, for example, near the interfaces of the layered medium. The additional contributions to the mass and stiffness matrices they incur can be evaluated analytically. This is a significant advantage over alternative approaches to enrichment where computationally complex and intensive high-order quadrature rules can be required for evaluating properly the contributions of the enrichment functions. Like all the previously developed DGM elements with Lagrange multipliers, the new DGM elements designed in this paper can be applied on non-matching meshes.

While the elements have been demonstrated here for planar interfaces, they readily generalize

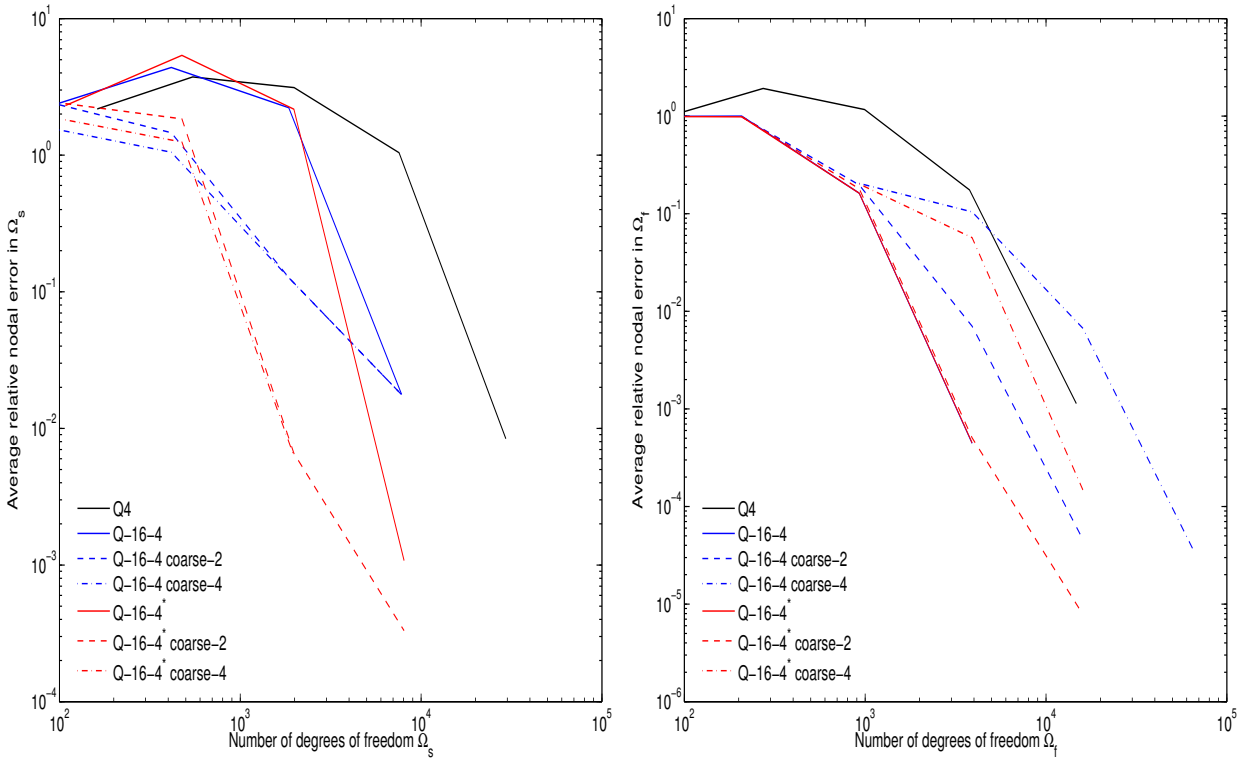

Fig. 20. Fluid/solid model wave propagation problem: performance comparison of Q-16-4*, Q-16-4, and Q_2 in Ω_s (left) and Ω_f (right) for $k = 160$, $k_p = 42.34$, and $k_s = 75.43$. The plotted error is the average of the relative errors obtained for $1^o \leq \theta_{\text{inc}} \leq 90^o$.

to smooth curved interfaces by working in a local frame near the interface. This will be addressed in an upcoming paper. There are several other areas that are still subject to further research, for example, non-smooth interfaces and interfaces with corners, optimal and/or automatic selection of the enrichment functions and Lagrange multipliers.

Acknowledgements

The authors acknowledge the support by the Office of Naval Research under Grant N00014-05-1-0204-1.

References

[1] C. Farhat, I. Harari and L.P. Franca. The discontinuous enrichment method. *Comput. Methods Appl. Mech. Engrg.*, **190**:6455–6479, 2001.

[2] C. Farhat, I. Harari and U. Hetmaniuk. A discontinuous Galerkin method with Lagrange multipliers for the solution of Helmholtz problems in the mid-frequency regime. *Comput. Methods Appl. Mech. Engrg.*, **192**:1389–1419, 2003.

[3] C. Farhat, I. Harari and U. Hetmaniuk. The discontinuous enrichment method for multiscale analysis. *Comput. Methods Appl. Mech. Engrg.*, **192**:3195–3210, 2003.

[4] C. Farhat, R. Tezaur and P. Weidemann-Goiran. Higher-order extensions of a discontinuous Galerkin method for mid-frequency Helmholtz problems. *Int. J. Numer. Meth. Engng.*, **61**:1938–1956, 2004.

[5] C. Farhat, P. Wiedemann-Goiran and R. Tezaur. A discontinuous Galerkin method with plane waves and Lagrange multipliers for the solution of short wave exterior Helmholtz problems on unstructured meshes. New computational methods for wave propagation. *Wave Motion*, **39**(4):307–317, 2004.

[6] L. Zhang, R. Tezaur and C. Farhat. The discontinuous enrichment method for elastic wave propagation in the medium-frequency regime. *Int. J. Numer. Meth. Engng.*, **66**:2086–2114, 2006.

[7] R. Tezaur and C. Farhat. Three-dimensional discontinuous Galerkin elements with plane waves and Lagrange multipliers for the solution of mid-frequency Helmholtz problems. *Int. J. Numer. Meth. Engng.*, **66**:796–815, 2006.

[8] P. David and J. Voge. *Propagation of Waves*. Pergamon Press, 1969.

[9] I. Tolstoy. *Wave Propagation*. McGraw-Hill Book Company, 1973.

[10] M. Roseau. *Asymptotic Wave Theory*. North-Holland Publishing Company, 1976.

[11] K.F. Graff. *Wave Motion in Elastic Solids*. Dover, New York, 1991.

[12] J.A. DeSanto. *Scalar Wave Theory*. Springer-Verlag, 1992.

[13] A. Bedford and D.S. Drumheller. *Introduction to Elastic Wave Propagation*. John Wiley & Sons, Inc., 1994.

[14] F. Ihlenburg. *Finite Element Analysis of Acoustic Scattering*. Springer, 1998.

[15] J. Billingham and A.C. King. *Wave Motion*. Cambridge University Press, 2000.

[16] T. Hunt. What Everyone Needs to Know About Evanescent Fields. *http://www.physics.harvard.edu/ tomhunt/pubs/evanescent.pdf*, 2003.

[17] F. Fornel. *Evanescent Waves: From Newtonian Optics to Atomic Optics*. Springer, 2002.

[18] L.L Thompson, S. Sankar and Y. Tong. Complex wave-number dispersion analysis of stabilized finite element methods for acoustic fluid - structure interaction. *Proceedings of SECTAM-XX*, :1–9, 2000. April 16-18, Callaway Gardens, GA.

[19] G. Barbastathis. Optics Course Notes. *http://web.mit.edu/2.710/www/*, 2002.

[20] M.K. Hong, A. Swan and S. Erramilli. Evanescent wave vibrational microscopy. *Optics & Photonics News*, (July):30–35, 2004.

[21] *http://www.mtronpti.com*.

[22] H.J. Simpson and B.H. Houston. Laboratory measurements of sound scattering from a buried sphere above and below the critical angle. *J. Acoust. Soc. Am.*, **113**(1):39–42, 2003.

[23] J. M. Melenk. *On Generalized Finite Element Methods*. Ph.D. Thesis, University of Maryland, College Park, MD, 1995.

[24] T. Strouboulis, K. Copps and I. Babuška. The generalized fintie element method. *Comput. Methods Appl. Mech. Engrg.*, **190**:4081–4193, 2001.

[25] T. Strouboulis, L. Zhang and I. Babuška. p-version of the Generalized FEM using mesh-based handbooks with applications to multiscale problems. *Int. J. Numer. Meth. Engng.*, **60**:1639–1672, 2004.

[26] T. Strouboulis, L. Zhang, D.L. Wang and I. Babuška. A posteriori error estimation for generalized finite element methods. *Comput. Methods Appl. Mech. Engrg.*, **195**:852–879, 2006.

[27] C. Daux, N. Moës, J. Dolbow, N. Sukumar and T. Belytschko. Arbitrary branched and intersecting cracks with the extended finite element method. *Int. J. Numer. Meth. Engng.*, **48**:1741–1760, 2000.

[28] T. Belytschko, C. Parimi, N. Moës, N. Sukumar, and S. Usui. Structured extended finite element methods for solid defined by implicit surfaces. *Int. J. Numer. Meth. Engng.*, **56**:609–635, 2003.

[29] C.A. Duarte and J.T. Oden. An hp adaptive method using clouds. *Comput. Methods Appl. Mech. Engrg.*, **139**:237–262, 1996.

[30] J. T. Oden, C. A. Duarte, and O. C. Zienkiewicz. A new cloud-based hp finite element method. *Comput. Methods Appl. Mech. Engrg.*, **153**:117–126, 1998.

[31] P. Monk and D.Q. Wang. A least-squares method for the Helmholtz equation. *Comput. Methods Appl. Mech. Engrg.*, **175**:121–136, 1999.

[32] T. Huttunen, P. Monk, F. Collino and J.P. Kaipio. The ultra-weak variational formulation for elastic wave problems. *SIAM J. Sci. Comp.*, **25**(5):1717–1742, 2004.

[33] P. Ladevèze and H. Riou. Calculation of medium-frequency vibrations over a wide frequency range. *Comput. Methods Appl. Mech. Engrg.*, **194**:3167-3191, 2005.

[34] R.A. Adams. *Sobolev Spaces*. Academic Press, New York, 1975.